Transverse Mass Dependence of Boson Interferometry in Heavy Ion Collisions at the CERN SPS.

by

Rama Jayanti

B.S. in Physics, 1988

M.S. in Physics, 1990

Submitted to the Graduate Faculty
of the Department of Physics and Astronomy
in partial fulfillment of
the requirement for the degree of
Doctor
of
Philosophy

University of Pittsburgh

December 8, 1995

Signed________________________

ACKNOWLEDGMENT

I would like to thank all the members of the NA44 experiment and all the physicist and technicians involved with the CERN SPS from where the data for this thesis was collected.

In particular, I would like to thank Prof T. Humanic for his patience and advice over the past four years. In addition I would like to thank B.V. Jacak, C. Fabjan, H. Boggild, B. Lorstad, B. Willis, T. Sugitate, A. Sakaguchi and K.Wolf for their guidance and help. I would also like to thank J. Sullivan for all his patience while teaching me Geant, Hubert and Gilbert for their help with the NA44 software , Y. Y. Lee for helping me get started in NA44, Sanjeev for answering my numerous questions and helping me at different stages of the thesis, Hal for getting me started on the On-line programs, Achim for all his help in the counting room, Jehanne for helping me learn the tedious Single particle analysis and many interesting shopping trips together, Jerry for his help with the Monte Carlo and of course for many a memorable hikes together in the Alps, Doug for discussions, Michael for all the normalization issues and Nu for attending to my numerous questions. I would like to thank ShinIchi for his help on calibrations, Shunji for the introduction to the hodoscope hardware in NA44 and Nobu for his questions and for all his help on my very first NA44 shift. Barbara H, Max, Shasha, Janus for all the good times in the counting room. A special thanks to Marko for many good times in the counting room and in St. Genis , where I learnt the intricacies of Austrian baking. Then there are many others whom I met in Geneva, Pittsburgh, Columbus and Tucson during my graduate student days who made the whole thing worthwhile. I would like to thank Reva for proof reading the thesis and Jignesh for all his help.

I would like to thank my family for all their support and guidance without which this thesis would be incomplete. Finally I would like to thank my husband , Ranjeev, without his constant help and support, this thesis would have remained a dream! I would like to dedicate this thesis to my parents for all that they have done for me.

ABSTRACT

First results of the transverse mass, m_T, dependence of $\pi^+\pi^+$ and K^+K^+ correlations from S + Pb collisions at 200 GeV/c per nucleon measured by the focusing spectrometer of the NA44 experiment at CERN are presented. Multi-dimensional fits characterize the pion and kaon emission volume. The pion radius parameter decreases with increasing p_T. Furthermore, the pion and kaon radii show a common $1/\sqrt{m_T}$ dependence. This behaviour can be interpreted as a result of a strong momentum-position correlation arising from collective flow. Further, a way to determine source sizes from deuterons is studied and compared with the source sizes obtained from HBT.

TABLE OF CONTENTS

LIST OF TABLES

LIST OF FIGURES

CHAPTER I. SUMMARY OF THE THESIS

The aim of Relativistic Heavy Ion Collisions is to study the hot and dense matter that is formed when high energy nuclei collide. The hope is to create a new state of matter, namely, the Quark-Gluon Plasma.

The new state of matter created can be detected by studying various signatures that have been predicted by different models. Enumerated below are a few of the possible signatures that various experiments are designed to study.

A. Transverse Momentum spectra and high Temperature Region

The transverse momentum of the particles is closely related to the global collision information, such as degree of thermalization achieved or the relative abundance of produced particles in A+A compared with p+p collisions. Besides providing global information on the hot compressed state of matter formed, in relativistic heavy ion collision, transverse momentum distributions of the particles are used as a probe of possible QGP formation. The study of p_T distributions as a QGP probe involves the investigation of collective effects, high p_T hadron productions, low p_T pion enhancement, and p_T as a function of energy densities. Collective flow of particles during the expansion of the hot dense matter is a non-thermal process that would indicate a significant departure from thermal models of the collision. The slopes of the transverse mass distribution would be significantly influenced by such flows. A low p_T rise was reported by NA35 with negative particles and has been of considerable interest to the Heavy Ion community since the ISR days. The low p_T rise could be indicative of exotic phenomenon such as plasma droplet formation. More mundane explanations arise due to the fact that there is an inherent phase-space bias along with significant rescattering and cascading of the produced particles especially at the target rapidities. Similarly a high p_T rise is of considerable importance since it is indicative of collective effects. High p_T excess or Cronin effect may be due to the multiple scattering of partons before hadronization [LP83], each parton picking up a little extra p_T at the expense of p_l, which gets transmitted to the hadrons and shows up as an excess of hadrons at higher p_T. However, this effect can be understood in terms of rescattering of formed pions with the target spectator nucleons.

B. Strange Particle Enhancement

Both at CERN and AGS energies, there is considerable interest in the study of strange particle enhancement. The enhancement is studied by comparing the kaon/pion (k/π) particle production ratio from A+A collisions with p+p collisions. There are five different factors contributing to the strange particle enhancement in nuclear collisions involving formation of QGP [ER91]: due to chiral symmetry restoration, the strange mass threshold is $3m_s \approx 300$, higher strangeness production rates in QGP, the large ratio of antistrange quarks $\bar{s}$ to light antiquarks $\bar{q}$, a high $s\bar{s}$ quark pair density in the QGP, and finally, because there are more channels for interaction (namely gluon-gluon) the strange particle content is expected to increase in advent of a QGP. The experimental evidence for strangeness signals is relatively recent. E802 reported a factor of 2 enhancement of the K^+/π^+ ratio while comparing Si+Au reaction to pA or pp reactions [A$^+$90, A$^+$91b]. The increase in K^+/π^+ is less significant within statistical error bars . At CERN energies, NA35 reported [B$^+$90] a factor of 2 enhancement in all neutral strange particles in the S+S collision as compared to p+p. NA34 [H$^+$91] has reported a gradual increase of up to a factor of 2 in K^+/π^+ ratios when going from p+p to p+W to S+W, where as they find that the K^-/π^- ratio is roughly constant. WA85 experiment has observed an increase in strange antibaryons, but the results suffer from limited statistics[A$^+$91a].

C. Long lifetimes and large Freezeout volumes

The lifetime and freezeout dynamics of the collision region is studied via the technique of HBT or Bose-Einstein Correlations. This technique was first used to determine stellar sizes in astronomy [HBT56]. The HBT effect arises from the interference of the matter waves of two identical particles as they are measured in coincidence since there are two possible paths for the particles to travel from the point of emission to the detectors. Forming a correlation function in terms of momentum difference between the identical particles allows estimation of the source size. At mid-rapidities transverse source sizes larger than the geometric dimensions of the incoming projectile have been measured [B+94a]. It has been predicted by various models that the formation of QGP leads to a very long-lived source[BGT88, BB89, Pra86a, Pra86b]. The Lifetime of the source can also be studied with HBT by studying the difference in energy between the two particles.

D. Enhanced Photon/Lepton Production

Photons and Leptons interact either through the weak or electromagnetic force; and hence they do not feel the strong force. Probes of this sort are indifferent to the hadronization mechanisms, decouple at early times, and are a direct measure of the hot dense matter. The measurement of real photons or lepton pairs is the only possible means of a direct access to the transient dense phase of matter. The direct or prompt photons and lepton pairs are produced by the process $q + \bar{q} \rightarrow \gamma$, $q+\bar{q} \rightarrow \gamma^*$, e^+e^-, $\mu^+\mu^-$ etc. A signature of QGP formation would be enhanced production of these direct photons and lepton pairs since large number of $\bar{q}$ pairs are produced in a phase transition.

E. J/Ψ Suppression

It has been predicted that the formation of QGP would lead to the suppression of the resonance J/Psi. The J/Psi resonance is formed by the combination of $c\bar{c}$ pairs. In a QGP, there is a Debye screening due to the excess free quarks that reduces recombination of $c\bar{c}$ pairs. Due to the abundance of various other lighter quarks, the c quark pairs up with the lighter u or d quarks forming a D meson and hence leading to a suppression of J/Psi.

F. Goal of the thesis

Amongst the many signatures that model calculations predict, NA44 is optimized to study the source size and the lifetime of the Collision region as mentioned above. It is predicted that in advent of a QGP formation, the lifetime of the source would be very large since the system spends a long time in the mixed phase and hence the hadronization times are long.

The purpose of this thesis is to study the collision dynamics using the technique of Intensity Interferometry or HBT. HBT is a technique used to measure source sizes which are developed by Hanbury-Brown and Twiss. Details of this technique are presented in chapter 3 and chapter 5. The radii, extracted using the technique of HBT, give us a measure of the spatial and temporal extent of the collision region. According to Pratt and Berstch [BB89, Pra86a] in advent of a QGP, the two transverse radii measured would be very different and much larger than what one would expect in case of a hadron gas. As illustrated in the Figure I-1, there are two scenarios that are possible. The collision of the nuclei can lead to either the formation of a hadron gas or to the QGP. The hadron gas formation would result in the two transverse radii, R_{t_s} and R_{t_o}, being equal since the same kinematics drive the motion of the particles in the two directions. On the other hand in advent of a QGP, owing to the large amount of latent heat, the system takes a long time to hadronize and hence the two transverse radii measured would be very different. (R_{t_o} would be much larger than R_{t_s}). I shall revisit this point in Chapter 5 after presenting the data.

In this thesis, a study of the transverse mass/momentum dependence and directional dependence of the HBT radii are made. The transverse mass ($m_T = \sqrt{p_T^2 + m^2}$, where p_T is the mean transverse momentum and m is the mass of the particle) dependence of the radii has been predicted for an expanding system by various models. The goal of the thesis is to study the transverse mass dependence of the HBT radii in order to understand the dynamical aspects of the collision. The various trends seen in data along with the interpretation is presented in Chapter 5 of this thesis.

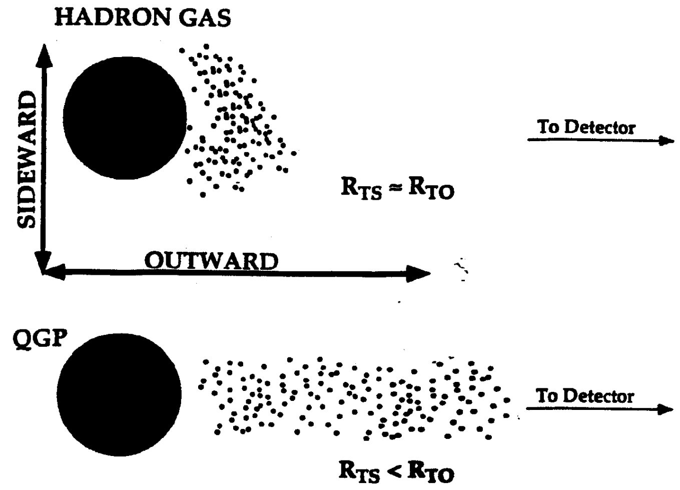

Two scenarios of the pion source function in the interferometry. The upper figure shows the source when there is no high density phase. The dots show the point of last interaction of pions of a given momentum. Their momentum correlation will reflect the space-time distribution of the source. The lower figure shows the spatial distribution of pions (of a given momentum) emerging from a source if there is a high density phase. The horizontal elongation is due to the time delay converting high density matter to the low density phase,
(G.F.Bertsch, Pion Interferometry, Nucl.Phys. A498 (1989) 173c-180c)

Figure I-1. Model predictions of the different possible scenarios in a Heavy Ion Collision.

CHAPTER II. Introduction

With the advent of ultra-relativistic heavy-ion collisions in the laboratory, at Brookhaven and CERN, a new interdisciplinary field has emerged from the traditional domains of particle physics and nuclear physics [Sch92]. In combining methods and concepts from both areas, the study of heavy-ion reactions at very high energies (E/m >> 1) denotes a new and original approach in investigating the properties of matter and its interactions. In high-energy physics, interactions are derived from first principles (gauge theories), and the matter concerned consists mostly of single particles (hadrons/quarks). Combining the elementary-interactions aspect of high-energy physics with the macroscopic-matter aspect of nuclear physics, the subject of heavy-ion collisions is the study of bulk matter consisting of strongly interacting particles (quarks/hadrons). The energy scale is given by the pion mass, or the limiting "Hagedron temperature", which roughly set around the pion mass. The physics is therefore inherently the physics of 'soft' processes and the objects under study are the hadrons ($\pi, K, \rho, p...$) and the light quarks (u,d,s). The predictions of QCD that at high energy densities matter should undergo phase transition to an entirely new state, the quark-gluon plasma (QGP) makes this field very interesting. At low energy densities, quarks and gluons are bound by strong force into colorless objects, the hadrons (confinement). In addition, the quarks acquire a large effective mass ($m_u \approx m_d \approx 300MeV, m_s \approx 500MeV$) via interactions between themselves and the surrounding physical vacuum (broken chiral symmetry). when increasing the energy density by increasing the temperature ('heating') or the matter density ('compression'), a phase transition might occur towards the QGP, the true perturbative vacuum of QCD, where partons are deconfined and chiral symmetry is approximately restored ($m_u \approx m_d \approx 5MeV, m_s \approx 150MeV$) .

Nuclei are extended objects, and therefore their geometry plays an important role in heavy-ion collisions. Figure II-1 shows a sketch of a reaction between two nuclei followed by the evolution of the reaction region; the nucleons can be separated into participants, with primary nucleon-nucleon collision, and spectators, which proceed with little perturbation along the original direction. In the first instance of the reaction, the nucleon-nucleon collisions between the two highly Lorentz-contracted nuclei redistribute a fraction of the original beam energy into other degrees of freedom. After a short time, usually taken to be of the order of 1 fm/c, partons materialize out of the highly-excited QCD field, possibly in the state of an equilibrated QGP. The system expands rapidly, mainly along the longitudinal direction, hence lowering its temperature, and reaches the critical transition temperature T_c after a few fm/c. Potentially, the matter then spends a long time (6 - 10 fm/c) in the mixed phase, in particular if the transition is of first order. The mixed phase has to rearrange the many degrees of freedom of the QGP into fewer available in the parton phase, with an associated large release of latent heat. In the last and hadronic phase, the still-interacting system keeps expanding, maybe even in an ordered motion ('collective flow'), to a very large dimensions until 'freeze-out' occurs, when interactions cease and the particles stream freely away to be detected in experiments. The space-time extent of the sources emitting radiation or particles can, in principle, be measured via intensity interferometry. The purpose of this thesis is to study the spatial and temporal extend of the source via the method of intensity interferometry.

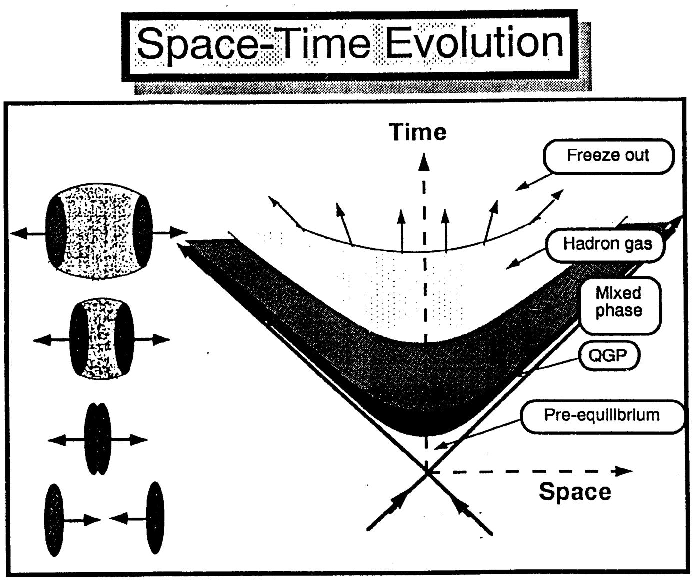

Figure II-1. The space-time evolution of the Nuclear reaction region.

CHAPTER III. Theory and Motivation

The technique of Intensity Interferometry was developed by Hanbury-Brown and Twiss (HBT) in the 1950's, as a means of determining the dimension of distant astronomical objects [HB+52]. They first used the technique of HBT to examine radio-wave sources in the galaxies Cygnus and Cassiopea and subsequently applied the method to a measurement of the angular diameter of Sirius [HBT56].

A. Amplitude and Intensity Interferomtery

The difference between *intensity* interferometry (HBT) and conventional *amplitude* interferometry is illustrated in Figure III-1. A finite-size source emits indistinguishable particles from positions r_1 and r_2 and the particles are observed at positions X_1 and X_2. Both emission points contribute to both observation points since they are Bosons.

In *amplitude* interferometry each of the "detectors" at X_1 and X_2 could be a slit through which the emitted particles pass. The particles could then produce an interference pattern, on a screen located on the opposite side of the slits from the source. The interference pattern so produced depends on the relative phase of the particles' amplitudes as measured at X_1 and X_2.

In *intensity* interferometry a correlation function is constructed from the number of counts n_1 and n_2 measured at X_1 and X_2 as

$$R(r_1, r_2) = (< n_{12} > / < n_1 >< n_2 >) - 1, \tag{III-1}$$

where n_{12} denotes the number of counts in which particles are observed at X_1 and X_2. The correlation function is proportional to the intensity of the particles at X_1 and X_2. Because of the symmetrization (or antisymmetrization) of the particle's wave function, identical particles can have a nonzero correlation even if the particles are otherwise noninteracting.

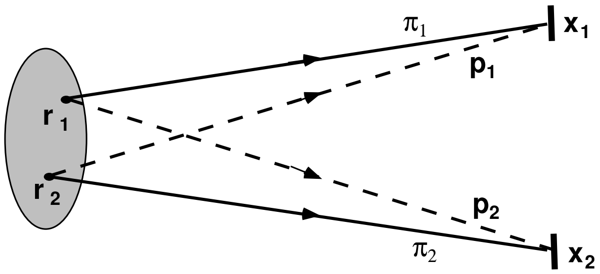

Figure III-1. Derivation of the Bose-Einstein Correlation Function.

B. Derivation of Bose-Einstein Correlation function

Assume two identical pions are emitted with four-momenta p_1 and p_2 at points r_1 and r_2 by a source $\rho(r)$ extended in space and time. Let the detection points detecting the pion with momentum p_i be denoted as X_i. If we assume that the particles behave as plane waves then the amplitude of this event is given by

$$A_{12} = \frac{1}{2}[e^{ip_1\cdot(X_1-r_1)}e^{ip_2\cdot(X_2-r_2)} + e^{ip_1\cdot(X_1-r_2)}e^{ip_2\cdot(X_2-r_1)}] \qquad \text{(III-2)}$$

The second term is required since pions are indistinguishable. The probability for such an event to occur is given by the complex square of A_{12} , integrated over all points,

$$\mathcal{P}_{12} = \int d^4r_1 d^4r_2 |A_{12}|^2 \rho(r_1)\rho(r_2) = 1 + |\tilde{\rho}(Q)|^2 \equiv C_2(\vec{Q}, Q_0) \qquad \text{(III-3)}$$

assuming that the production amplitudes are independent of r and uncorrelated.

Equation II-3 is the fundamental result of intensity interferometry. It states that the two-particle counting rate is proportional to the square of the Fourier transform of the source distribution function. The Fourier transform is performed with respect to the relative four-momentum of the particles, with each component of relative momentum containing information of the source distribution in the conjugate spatial variable. The range of enhancement in the i-th component $\vec{Q}_i$ is of the order of $1/R_i$, where Q_i is the four-momentum difference vector of the particles. If the source distribution is a gaussian in space-time, then the correlation function is given by

$$C_2(Q) = 1 + e^{-\vec{Q}^2\vec{R}^2 - Q_0^2\tau^2}; \rho(\vec{r}, t) \equiv e^{-\vec{r}^2/2\vec{R}^2 - t^2/2\tau^2} \qquad \text{(III-4)}$$

However, it is seen in experiments that even though $Q \to 0$, $C(Q) \neq 2$. Hence one introduces a parameter λ also referred to as "coherence parameter" in equation II-4. It is interesting to note that various dynamical processes affect the λ parameter, the details of which will be discussed in the following sections.

C. Coherence

Suppose that the particles are emitted from a source with probability amplitude f_i, then the total probability $P(p)$ of observing the particle with momentum p from these sources is given by either $P_c(p) \sim |\sum_i \Psi(x_i) f_i|^2$ for coherent sources or by $P_I(p) \sim \sum_i |\Psi(x_i) f_i|^2$ for incoherent sources. Suppose further that the source is continuous in space so that the summation can be replaced by an integral and that the particles are plane waves i.e. $\Psi_p(x) \sim exp(ipx)$ then

$$P_c(p_1, p_2) = \frac{1}{2} | \int d^4x_1 d^4x_2 \Psi_{12}(x_1, x_2) f_c(x_1) f_c(x_2)|^2 \tag{III-5}$$

$$= \frac{1}{2} | \int d^4x_1 d^4x_2 \frac{1}{\sqrt{2}} (e^{ip_1 \cdot x_1} e^{ip_2 \cdot x_2} + e^{ip_1 \cdot x_2} e^{ip_2 \cdot x_1}) f_c(x_1) f_c(x_2)|^2 \tag{III-6}$$

$$= |\tilde{f}_c(p_1) \tilde{f}_c(p_2)|^2 \tag{III-7}$$

Here the tilde denotes a Fourier transform. For a coherent source the correlation function defined in Equation 7 reduces to 1. For an incoherent source P_I is given as

$$P_I(p_1, p_2) = \int d^4x_1 d^4x_2 |\Psi_{12}(x_1, x_2) f_I(x_1) f_I(x_2)|^2 \tag{III-8}$$

$$= |\tilde{F}_I(0)|^2 \pm |\tilde{F}_I(p_1 - p_2)|^2 \tag{III-9}$$

where $F_I \equiv f_I(x)^* f_I(x)$. P_I has no dependence on the total momentum but there is a correlation between the two individual momenta. It is from such incoherent sources that correlation can arise. If different parts of the source emit particles coherently, the two-particle correlation function in momentum vanishes.

The problem of coherence can be approached by the following argument. The coherent sum $P_c(p) = |\sum_i \Psi(x_i) f_i|^2$ can be expanded as

$$P_c(p) = \sum_i |\Psi(x_i)|^2 |f_i|^2 + \sum_i \sum_{i \neq j} \Psi(x_i) \Psi^*(x_j) f_i^* f_j \tag{III-10}$$

where the first term on the right hand side is the contribution from the incoherent part of the source. Thus for $P_c(p)$ to behave like a completely incoherent sum it is necessary for the cross-terms to vanish.

One may consider the vanishing of the cross-terms as arising from averaging over some quantity or quantities. If the f_i fluctuate randomly in the variables being averaged over, then the average will tend to be small. The elimination of cross-terms is often referred to as "phase averaging" [GKW79, Shu73, Bow85]. Hence it is seen from the above discussion that one can go continuously from a coherent source to the incoherent source depending on the degree of orthogonality between the f_i.

D. Kinematical Correlations

The conservation of energy-momentum leads to kinematic constraints between the produced particles in heavy ion collisions. If one of the produced particles is near the kinematic limit then there is a very strong correlation between particles.

Conservation of internal symmetries and quantum numbers can also lead to correlations between particles. However, in Heavy-Ion collisions since many particles are produced and correlations between 2 or 3 particles is measured, the rest of the particles act as a reservoir against various kinematical boundaries.

Correlation between position-momentum can cause the source to "look" smaller. Some string dynamic models [Hof87] predict source size of about 20 fm along the beam directions but position-momentum correlations lead to sources of the order of a few fermis.

E. Final-State Interactions

Final state interactions arising from Coulomb interaction reduce the value of λ and also affect the radius parameter. It is well known that the solution of the Schrodinger's equation [Flü74] in a Coulomb potential modifies the two-pion relative momentum distribution according to

$$\frac{n_{\pm\pm}(Q)}{n_{oo}(Q)} = \frac{2\pi\eta}{e^{2\pi\eta}-1}; \eta = \frac{m_\pi e^2}{\hbar Q_{\pi\pi}} \qquad \text{(III-11)}$$

Where $Q_{\pi\pi}$ is the relative three-momentum of the two pions in their center of mass, m_π is the pion mass, e is the charge and $\hbar$ is Plank's constant. Corrections based on this formalism were first suggested by Gyulassy[GKW79] and applied to data by Zajc [Zaj82]. The implication for Bose-Einstein analysis is that these corrections can affect a large region of the relative momentum space. Such correlations are acceptance dependent and can produce a substantial change in the inferred values of R and λ.

The final state strong interactions between $\pi^\pm\pi^\pm$ also modifies the measured BE correlations [Bow90]. A recent calculation by Suzuki [Suz87] predicts that the s-wave phase shift varies slowly in the the range of $0 < Q < 1$ GeV, nonetheless a substantial modification in the value of λ is found, suppressing the true value by 20%.

Some of the ambiguity concerning the separation of the production dynamics from final-state interactions may be removed by the very nature of the spatially-extended pion source. In case of the two-pion Coulomb interactions, the source size leads to a correction factor or the order of $m_\pi R/137$ [GK81, Zaj82, PCZ90]. According to Bowler [Bow87] the effect of final state strong interaction is considerably modified, since the s-wave scattering length i$\sim$ -0.2, which is substantially smaller than the source sizes being measured by the BE correlations.

F. Resonance Production

One of the effects which is very important especially in case of the pions are the resonances [GP90]. A large fraction of the pions arise as decay product of long lived resonances such as $\rho, \omega, \eta, \eta'$.... etc. The ρ, with a width of 153 MeV, decays with in the source itself and hence has a negligible affect on the two-particle correlations, whereas the ω with life times of 20 fm leads to masking of the two-particle correlation function. A resonance with mass M and momentum $\overline{k}$ will travel a distance $\sim |\overline{k}|/$ τM before decaying, thereby creating an effective source from its decay products.

An event generator like RQMD predicts [Qua94] that about 23% of the low p_T ($p_T < 150$ MeV/c) come from decay of resonances, whereas only about 4% of the kaons result from resonance decays.

A large source produces BE enhancements at only very small momentum difference, much smaller than the experimental resolution of the detectors. If this narrow peak is not resolved, only the fraction f_d of the directly produced pions will interfere, leading to a value of $\lambda \sim f_d^2$.

One can in principle correct for this effect if one knows the various abundance of the different resonances and their primordial momentum distributions.

G. Event Classification

Most experiments average over events while constructing the correlation function. This can lead to a problem [GK81], since each event in itself might have a fluctuation given by $f(\sigma) \sim e^{-\sigma^2/2\beta^2}$. If the source distribution is assumed to be a gaussian given by $\rho(r) \sim e^{-r^2/2\sigma^2}$ then averaging over events leads to source distribution

$$\rho(r) = \int f(\sigma)\rho_1(r : \sigma)d\sigma \tag{III-12}$$

which would lead to a correlation function of the form $C_2(Q) = 1/(1 + \beta^2 Q^2)$. Attempting to fit this with a gaussian would lead to a distorted value of λ.

H. Experimental Acceptance

The experimental acceptance can further distort the measured value of R and λ. If the experimental acceptance is such that the acceptance is, say, mainly in one of the components of Q, the measured R is conjugate to that component of Q, i.e. if one resolves Q into its components Q_x, Q_y, Q_z and the spectrometer acceptance is such that only Q_y is accepted then the measured R corresponds to R_y and not to the full R.

I. Contamination

The pion pair sample could be contaminated by kaons or other particles . If, say, x% of the pions are actually kaons then $(1-x)^2$% of pions will have no BE correlations. In such cases, one underestimates the Coulomb effect since the mass of the kaon is larger than that of the pion.

If x% of the pions come from long-lived resonances then $(1-x)^2$% should not be Coulomb corrected. When pions arise as a decay product of the long-lived resonances one over estimates the Coulomb correction.

There was no attempt made in this thesis to correct for contamination of the pion data set with Kaons. But this correction would indeed be very small since the experiment NA44 has excellent particle-identification.

CHAPTER IV. The NA44 Experiment

NA44 is a second generation experiment benefitting from the earlier surveys. It is a focussing spectrometer which studies identified single particle inclusive spectra (π, K, p, d) and two particle correlations (π, K, p) at mid-rapidity. High statistics and good momentum resolution allow multi - dimensional parameterization for the two-particle correlation function. The spectrometer can trigger on one sign particle at a time. Systematic studies have been performed to look at centrality dependences, target dependences[Nis94] and transverse momentum dependences[B^+94b]. Finally since NA44 can identify the particles on-line we can trigger on rare particles like K^-K^-[Pan93].

The experiment is located in CERN, Geneva in the north hall, in the H4 beam line of the CERN SPS (super proton synchrotron) as seen in the Figure IV-1. NA44 has data from proton beam at 450GeV/c, Sulphur beam at 200 GeV/c and recently taken lead beam at 160 GeV/c. The beam intensities are roughly 1 million particles/ spill. The proton beam cycle was on for 2.5 seconds and off for 12 seconds. The Sulphur beam cycle was on for 5 seconds and off for 14 seconds. The beam spot size is roughly 2mm wide and about 5mm long.

The NA44 Focusing Spectrometer, show in Figure IV-2, [B^+93a] uses two dipole magnets and three quadrupoles to create a magnified image of the target on the focal plane of the hodoscope 1. There are three hodoscopes used for tracking. The beam passes through the cherenkov, which gives the start timing and then hits the target. Immediately after the target is the Silicon pad array which gives a measure of centrality along with the T0 counter. There are two threshold Cherenkov's which give on-line (and off-line) particle identification. Additional particle identification is given by the time-of-flight from the very last hodoscope. Finally the Uranium calorimeter provides e,π,μ rejection. There are four wire chambers which are used only as a means to provide absolute momentum calibration in conjunction with the third dipole.

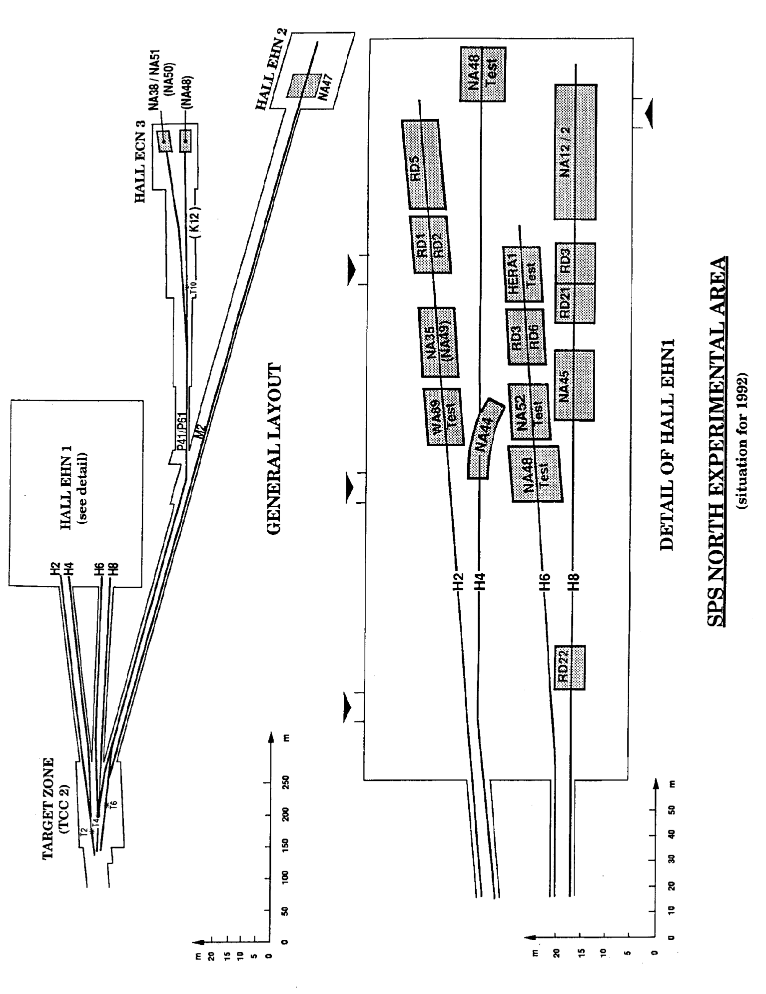

Figure IV-1. The SPS experimental Hall.

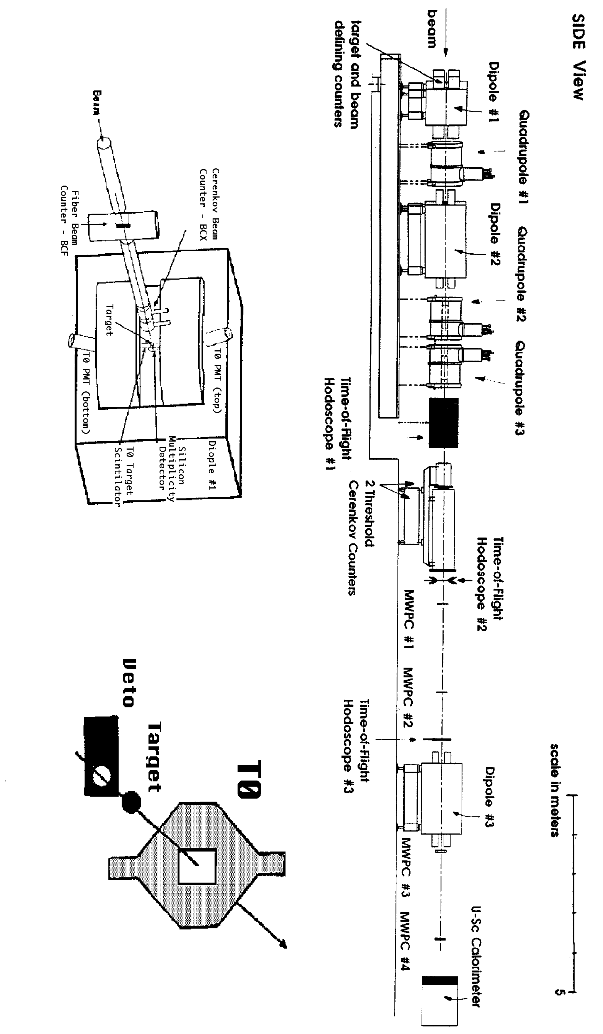

Figure IV-2. The NA44 experimental set-up.

A. Target

The target used in this thesis is 0.5 cm thick *Pb* corresponding to $\approx 3\%$ interaction length. Multiple scattering from the target is the main source of poor momentum resolution. Multiple scattering is directly proportional to the target thickness and inversely proportional to the momentum of the particles.

B. Beam Counter and/or Start Counters

During the Sulphur run, the beam rate and the start timing were both given by a gas cherenkov counter [$\mathrm{M}^{+}94$], called CX, located $\approx$ 50cm in front of the target. The detector consists of two radiator volumes CX1 and CX2 which independently measure the start timing of the particles. Each of the volumes are connected to photomultiplier tubes. The signal from each of the PMT is split, one signal going to the charge ADC's and the other connected to the TDC's via the discriminator. The signal is discriminated twice; once in the zone and once in the counting room to correct dispersion in the cable. The TDC's count in bins of 50 ps. The resolution of this detector is estimated to be $\approx$ 33ps [$\mathrm{M}^{+}94$].

The resolution however gets worse with increasing beam rate since this causes more than one particle to be within the trigger window causing large pulse heights and hence faster timing. This effect can be corrected by slewing corrections as will be discussed for the hodoscopes but the start counters are not corrected for it owing to the fact that the TOF resolution is dominated by the hodoscopes. The beam structure and high beam rates do often allow two or three beam particles to be with in the trigger gate, but such events can be thrown out offline. It is good to throw away multiple beam particles, since for the Bose-Einstein correlation function calculations it is necessary that both the particles originate from the same event.

During the proton run, since the protons do not cause enough light in the Cherenkov start counter, the start timing is given the T0 counter and the beam rate is given by the beam counter. The TOF resolution in this case is worse owing to the T0 resolution.

C. Veto Counters

In order to ensure that the beam travels fairly straight there are veto counters placed upstream of the target. There are three veto counters, one with a hole of radius 4mm placed 2cm in front of the target and two additional veto counters with 2mm radius holes placed on either side of the CX counter. The veto counters are part of the trigger and hence enable online and offline analysis of good events.

D. Interaction Counters

There are two detectors used by NA44 as interaction counters, the Silicon pad array and the T0 counter. Tagging on the impact parameter gives us systematic study of various quantities as a function of centrality. The Silicon pad array consists of 192 pads with an η (psuedo-rapidity) coverage 1.5 - 3.3 and phi acceptance of 2π. The detector has a 0.5 mm hole in the center and is about 300 μm thick. The segmentation of the detector is such that the η step is constant. The detector is segmented into 24 phis and 8 concentric rings. Each pad is connected to a pre-amplifier which is read out by charge integrating ADC 's. The signal-to-noise ratio is greater than 10. During the Sulphur beam about 5% of the pads were not functional. The spectrometer two-particle trigger is such that it is biased towards rather central events.

The T0 is a scintillator slat which is connected to a ADC and TDC via discriminator at the top and bottom end of the slat. From the amount of charge deposited one can get an idea of the impact parameter, since T0 is located immediately after the target and sees the full collision. A plot of the ADC distribution from the T0 is shown in figure IV-3.

E. Magnets

The NA44 Focusing spectrometer has three dipole magnets and three quadroples. The first dipole is used for separation of the primary beam from the secondary beam, allowing only the secondary beam into the spectrometer. The second dipole is used for momentum selection, namely, for selecting momenta between 2 to 8 GeV/c. The momentum range selected is $\pm$ 20 % of the nominal momentum setting. The third

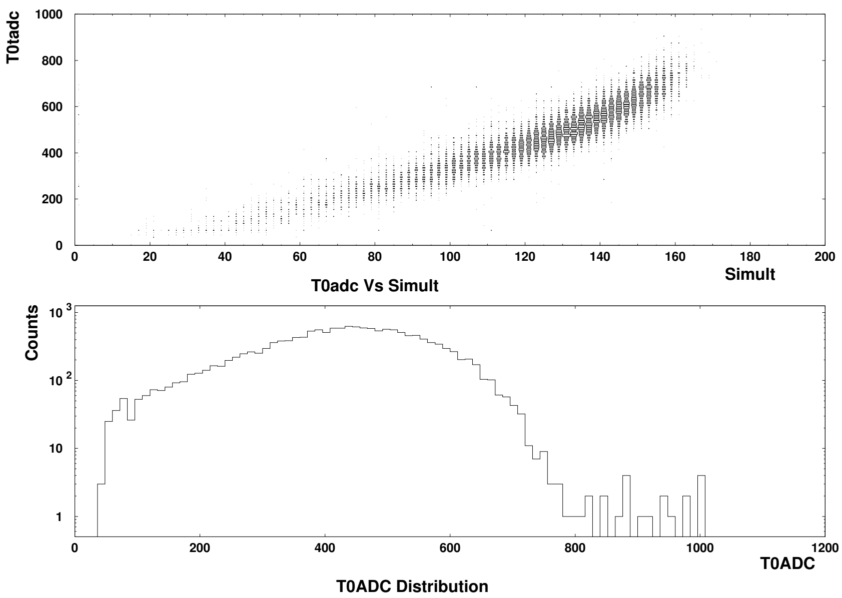

Figure IV-3. T0 Pulse Height distributions.

dipole is used mainly for the purpose of absolute momentum calibration. This is done in conjunction with the four wire chambers which are placed very close to D3. The three quadroples are used for focussing the particles on to the focal plane of the first Hodoscope. The spectrometer is run in two magnetic settings, referred to as the horizontal and vertical setting. These two settings together optimize the acceptance in px, py and pz. The acceptance of the spectrometer in the horizontal and vertical setting is shown in Figure IV-4. Figure IV-5 illustrates the transverse and total momentum distribution in the spectrometer for the 4GeV/c setting. The spectrometer is run in two angular settings, one at an angle of 44mrad w.r.t to the beam axis, referred to as the low p_T setting and the other at an angle of 131mrad w.r.t the beam axis which is referred to as the high angle setting. The NA44 acceptance in y-p_T for the low and the high angle settings for various momenta is shown in Figure IV-6.

F. Hodoscopes

The spectrometer has three highly segmented hodoscopes which are used for tracking and particle identification [KS90]. The dimensions of H1 (50 slats), H2 (60 slats),

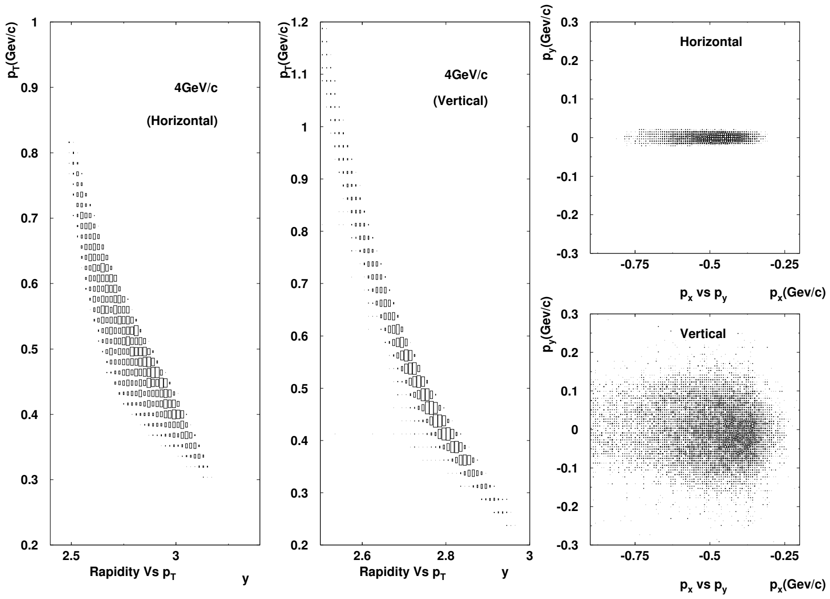

Figure IV-4. The NA44 Acceptance plots.

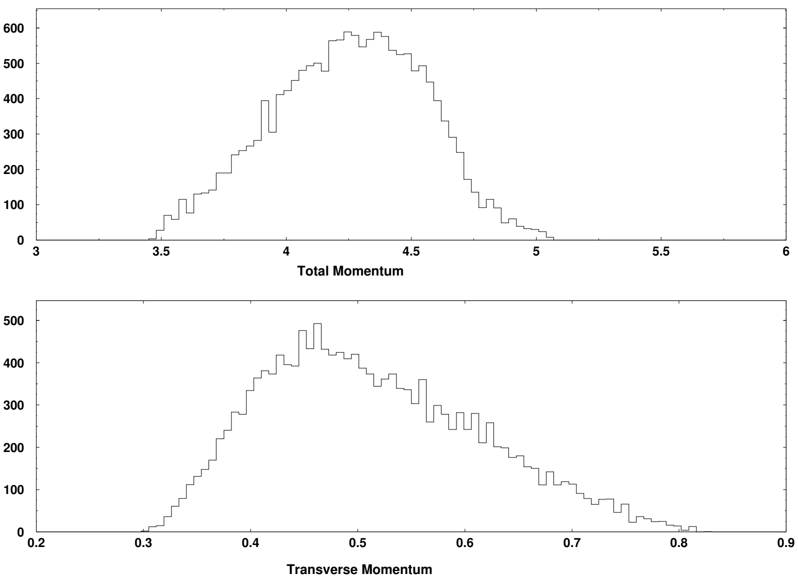

Figure IV-5. The NA44 Acceptance plots.

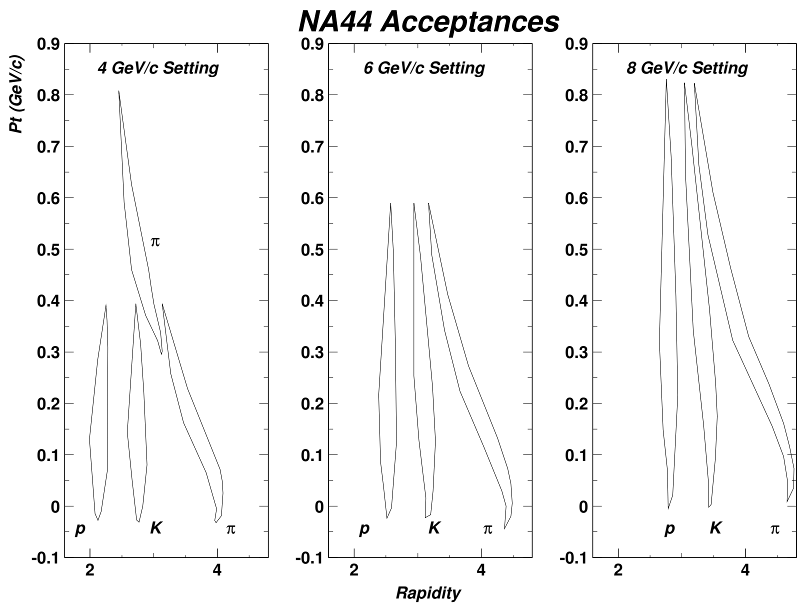

Figure IV-6. The NA44 Acceptance plots.

H3 (50 slats) are 28×1×260 mm, 6×6×200 mm, 13×10×220 mm (width×thickness×length). H1, H2, and H3 are located at 8.62m, 13.88m and 18.35m downstream of the target respectively. H1 is at an angle of 5 degrees to the central line while H2 and H3 are perpendicular to it. Each hodoscope consists of an array of scintillator slats which are connected to a photomultiplier tube at the top and bottom end of the scintillator slat. The signal from the PMT is then split, one signal goes to the ADC and the other to the TDC via a discriminator. From the hit positions on the hodoscopes the tracks are reconstructed by requiring straight line trajectories tracing back to the exit of Q3. The slat number gives the x-position, the resolution of which is set by the slat thickness. The y-position is determined by the difference in the top and bottom TDC values, the resolution of which is estimated to be 0.8 cm. The z-position is given by the position of the hodoscope itself. TOF information from H3 is used for particle identification since it is farthest from the target allowing better separation in time between the particles. One can combine TOF information with the momentum of the particle to calculate the mass squared plots for better Particle Identification by using

$$m^2 = p^2(t^2c^2/z^2 - 1) \qquad \text{(IV-1)}$$

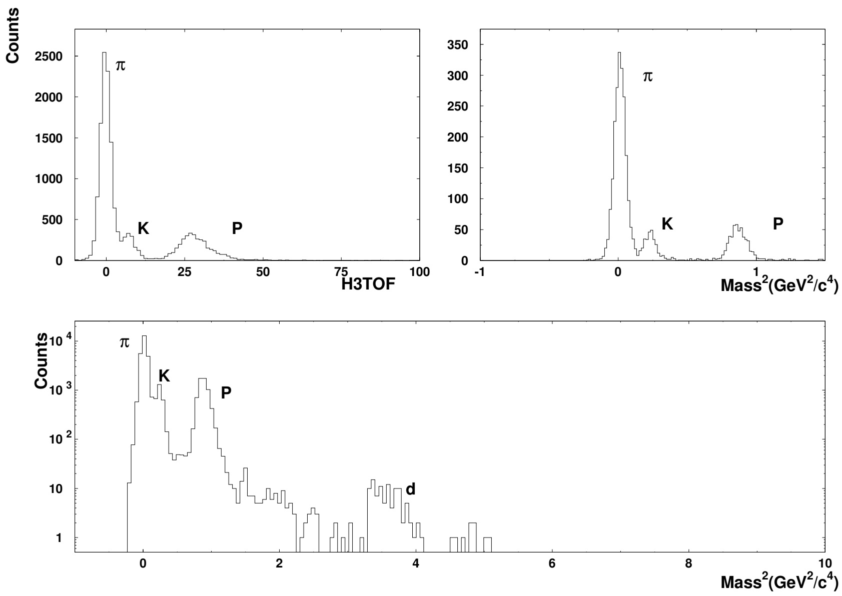

Figure IV-7. The TOF and Mass-squared Distributions at 4GeV/c Momentum setting.

$$(\Delta m^2)^2 = 4p^4(\frac{1}{\beta^4}(\frac{\Delta t}{t})^2 + \frac{1}{\beta^4}(\frac{\Delta z}{z})^2 + (\frac{1}{\beta^2} - 1)^2(\frac{\Delta p}{p})^2) \qquad \text{(IV-2)}$$

where m is the mass, p is the momentum, t is TOF, z is the flight path from the target to H3 and $\beta = z/\text{tc}$. Mass squared plots are used since finite resolution of the detectors causes particles to travel with speeds greater than the speed of light. One can estimate the resolution in mass squared spectra from the above plots. Monte Carlo simulations have shown that Δz variation due to flight path differences is less than 1 cm. $\Delta p/p$ is 0.2% leaving $\Delta t/t$ to be the main source of finite mass squared resolution. The main source of TOF resolution is thought to be the $\pm$ 2 volt fluctuation of the high voltage supply to the hodoscope photomultipliers [Pan93]. Mass squared is very useful for particle identification especially for the heavier mass particles and at higher momenta where TOF separation is poor since all particles travel with roughly the same speed at high momenta. The Figure IV-7 shows the mass-squared and TOF distribution of particles at 4GeV/c momentum. The plots indicate that the contamination of pion data set with kaons is less than a few %. The second plot in Figure IV-7 shows the good particle identification which allows physics analysis of rare particles like deutrons.

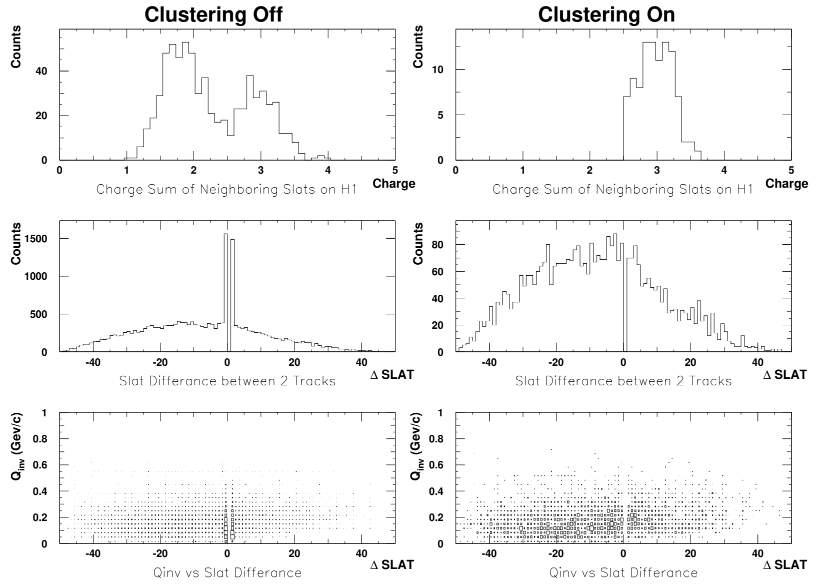

Figure IV-8. Q_{inv} distributions with and without Clustering.

Owing to the geometry of the H1, many single tracks hit two slats leading to spurious 2-track events. A clustering algorithm was used to get around the problem of single tracks hitting two adjacent slats. The adc sum of the two slats is compared to a preset value of the threshold. Depending on whether the sum is smaller or larger than the threshold one can determine if it is one track or two track event.

G. Cherenkovs

There are two Cherenkov counters placed after H1 as shown in Figure IV-2. They are used either in ignore, require or veto mode depending on the momentum setting and the particle type. C1 is used for π,k,p separation while C2 is used for e rejection. The number of photoelectrons produced increases with the radiator length. Hence at a given momentum setting the lighter particles require longer radiators than heavier particles. At threshold however the number of photoelectrons produced increases with momentum. The response of C1 as a function of momentum is shown in Figure IV-9. A Monte Carlo program mcherry was developed which simulated the behaviour of the Cherenkovs, including effects such as quantum efficiency of the tube and detector geometry. As seen from the figure at 4GeV/c, C1 is used in ignore mode since only

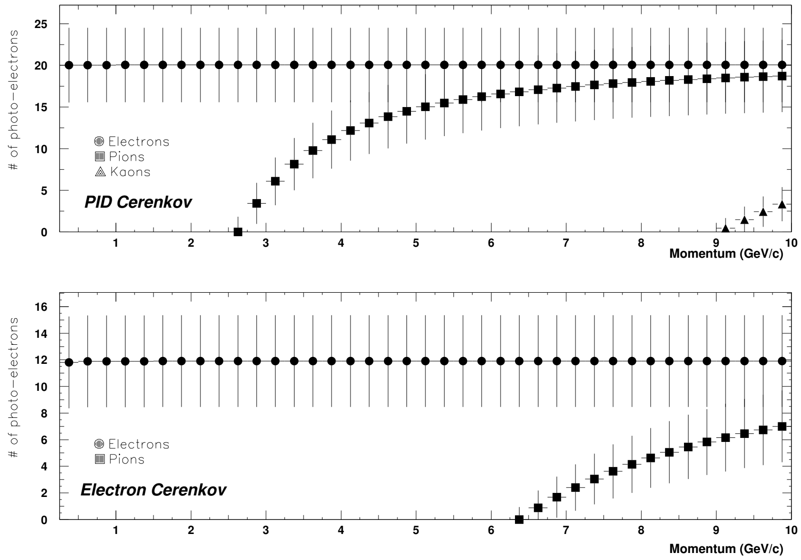

Figure IV-9. Monte Carlo predictions for the performance of the NA44 Cherenkov's.

the pions cause light in the counter and C2 is used in veto mode since only electrons fire this counter. Figure IV-10 shows the ADC distribution of the two Cherenkov counters at 4GeV/c momemtum setting. At 4 GeV/c setting, the k/p are in the pedestal of C1 and π are in the pedestal of C2.

H. Uranium-Copper Calorimeter

This detector (UCAL) is placed at the very end of the spectrometer and it consists of horizontally segmented 9 vertical stacks. The stacks are further segmented longitudinally into electromagnetic and hadronic sections. The electromagnetic section contains 2 mm uranium plates alternated with 2.5 mm scintillator and measures 6.4 radiation lengths or 0.23 interaction lengths. The hadronic section consists of 2.5 mm scintillator alternated with either 3 mm thick uranium plates or a combination of 3 mm thick uranium plates and 5 mm copper plates and are 4.0 and 3.8 interaction lengths deep respectively [SG90]. The choice of uranium as the passive medium allows for the construction of a compact calorimeter as well as equalizing the electromagnetic and hadronic response of the device [A+87]. The scintillators are read out on both sides by 6 independent 2 mm thick Plexiglass Wave Length Shifter

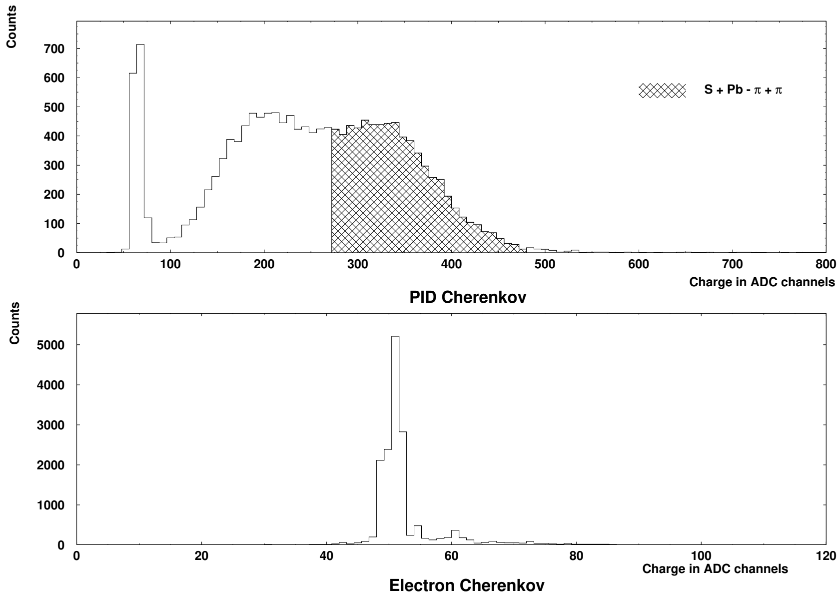

Figure IV-10. ADC distributions of the two Cherevkov counters.

Plates (WLS) creating a further vertical segmentation into 6 towers measuring 20 $\times$ 20 cm, the estimated size of a shower. The light in the WLS are read out by photomultiplier tubes which send signals to charge integrating ADC's in the counting room. The detector's acceptance is limited by dipole 3 which cuts into the y acceptance by 3 cm. The total y acceptance of H3 is 20 cm and the dipole 3 cuts only into the edge of the acceptance where there are few particles. The detection efficiency is about 85% [SG90]. The remaining 15% is mostly decays , interactions, garbage hits or misidentified tracks which are not within the UCAL acceptance. This detector can be used for separation of pions, muons and electrons but it was not used in this analysis. The electrons deposit most of their energy in the electromagnetic section of the detector while the hadrons deposit most of their energy in the hadronic part. By looking at the ratio of the electromagnetic energy to the total energy of the UCAL one can reject electrons very easily.

I. Wirechambers

There are four multi-proportional wire chambers in NA44 which are used only for determination of the absolute momentum scale, since they cover only part of the acceptance. Two of these are located before D3 and the remaining two are located after D3. Each chamber has 256 vertical anode sense wires and 96 cathode strips. The anode sense wires have a pitch of 2 mm and are 20 microns wide and 240 mm long. The cathode strips are 5 mm wide and 256 mm long. The anode sense wires provide the x information while the cathode strips provide the y information. The anode wires are read out by Lecroy PCOS electronics and the cathode strips by amplex.

J. Trigger

The basic trigger in NA44 is defined as

$$Trigger = GoodBeam + \begin{matrix} Min\ Bias \\ Central \end{matrix} + \begin{matrix} Track\ in \\ Spectrometer \end{matrix} + \begin{matrix} Cherenkov's\ in \\ correct\ state \end{matrix}$$

Signals from the beam counter, $\overline{VETO}$, T0, the three hodoscopes and the Cherenkov's are required in the coincidence. In the present set up of the spectrometer only signal from the top phototubes of the hodoscopes is required in the trigger. The trigger can be made cleaner by requiring the coincidence of both top and bottom phototube signals.

If the trigger accepts an event then it creates a 50ns window within which the ADC and TDC signals from the other detector elements arrive. In order to ensure that the next event is not accepted in the same trigger before all the detectors have relaxed to their ground state a 50ns after protection is defined. Similarly there exits a before protection window which is set to 50ns. Before protection is driven by the slowest detector in the spectrometer.

K. Data Acquisition and Monitoring

The DAQ and Monitoring was developed from a package called SPAW3 [Bek90] in an environment called MACUA1. This provides a fortran complier to run on the Macintosh computers. The fortran complier is often referred to as RTF (or real time fortran), which is fast fortran with additions like pointers, embedded assembler language statements etc.

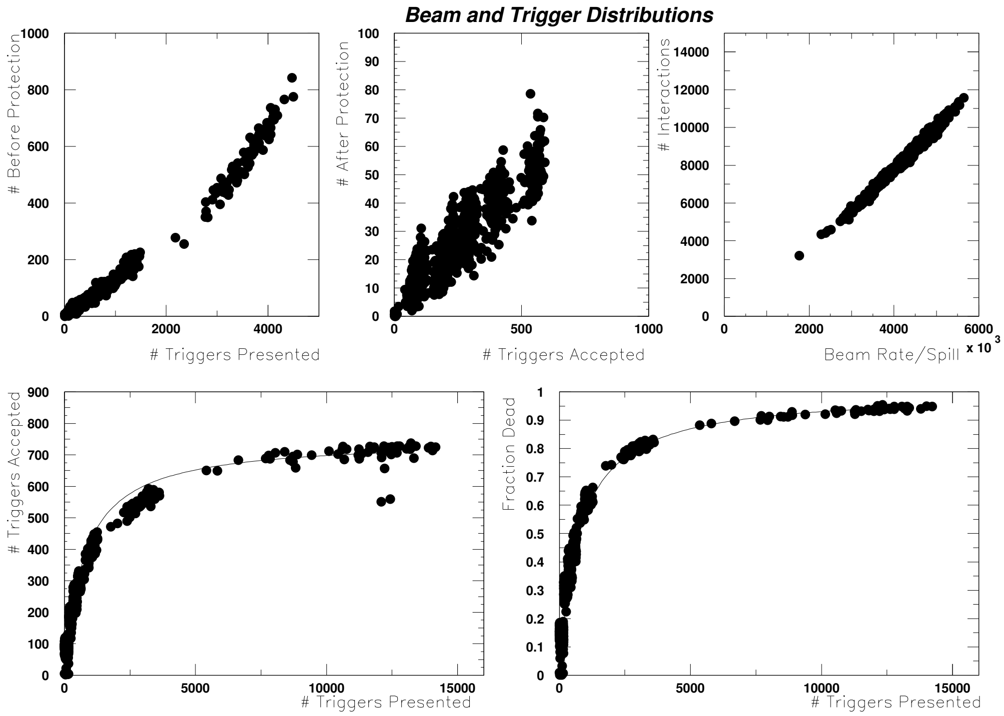

Figure IV-11. Correlations between DAQ and trigger related quantities.

The NA44 DAQ [Pan93] consists of series of M68xxx chips that share a common memory in the VME create. All the detectors are read out by CAMAC standard. The readout modules from various detectors sit in the CAMAC crate and appear in the address space of the M68xxx chips. The hand-shaking between the VME and the Macintosh is via the MICRON cards which sit in the nuBUS slots of the Macintosh. A schematic diagram of the DAQ is shown in Figure IV-12 and the address maps are shown in Figure IV-13. Each nuBuS slot provides 256 MBytes of external address space of which the VME crate takes up 16 Mbytes.

During the spill the DAQ requests a trigger and begins to read out the various elements once the trigger is accepted and waits for the next trigger. In between the spills the DAQ writes out the events to tape. Data are written to IBM 4280 cartridge drives at 200 Kbytes/sec.

The primary CAMAC modules used in Na44 are 11 bit 50ps/channel 8 input LeCroy 2228 TDC's, 11 bit 16 input LeCroy 2249 charge integrating ADC's for the target area, high density 48 input 12 bit LeCroy 228x charge integrating ADC's for the hodoscopes and the UCAL and peak sensitive ADC's for the Silicon pads. The 228x ADC have a slow conversion time of 1.5ms. The total read out time per event is roughly 6.5ms owing to the slow conversion time of the ADC's and the fact that the CAMAC read out time is ≈ 4 μs due to the 16 bit bus between the Macintosh and the VME crate.

The online monitoring system in NA44 also runs in the SPAW3 environment. It continuously monitors the events which are being read out by the DAQ. There are three Macintoshes which are used for different types of monitoring tasks. The MAC1 performs histogramming tasks (via the program SCANMAC.EXEC) and is also used for debugging purposes of the actual datastream (via DEBUG.EXEC). MAC2 is used for the purposes of event display (EVENTDISPLAY.EXEC) and also for controlling high voltage and to control the movable XY table. The MAC3 is used for continuous monitoring of events and at the end of each run it prints out automatically various quantities from different detectors, for e.g. the adc distributions, tdc distributions etc. In addition to this the MAC3 also scans on a continuous basis certain quantities like the Cherenkov pressure which need to remain constant throughout the run [J+93].

Some of the DAQ and trigger related diagrams are shown in Figure IV-11. There exists a linear relationship between the number of triggers presented to the number of before protection because the before protection is caused by the presence of a previous beam particle within 50 ns of the present trigger. Further, the number of after protections are caused by the presence of another beam particle within 50 ns of the trigger beam particle. As the beam intensity increases the non-linearity in the above relations increases as shown in Figure IV-11.

Not all triggers presented to the DAQ are read out due to the finite readout time of the DAQ. The number of triggers presented and the number of triggers accepted are related by the equation

$$\frac{1}{T_{presented}} = \frac{1}{T_{accepted}} - \frac{1}{T_{max}} \qquad \text{(IV-3)}$$

where T_{max} is approximately 750.

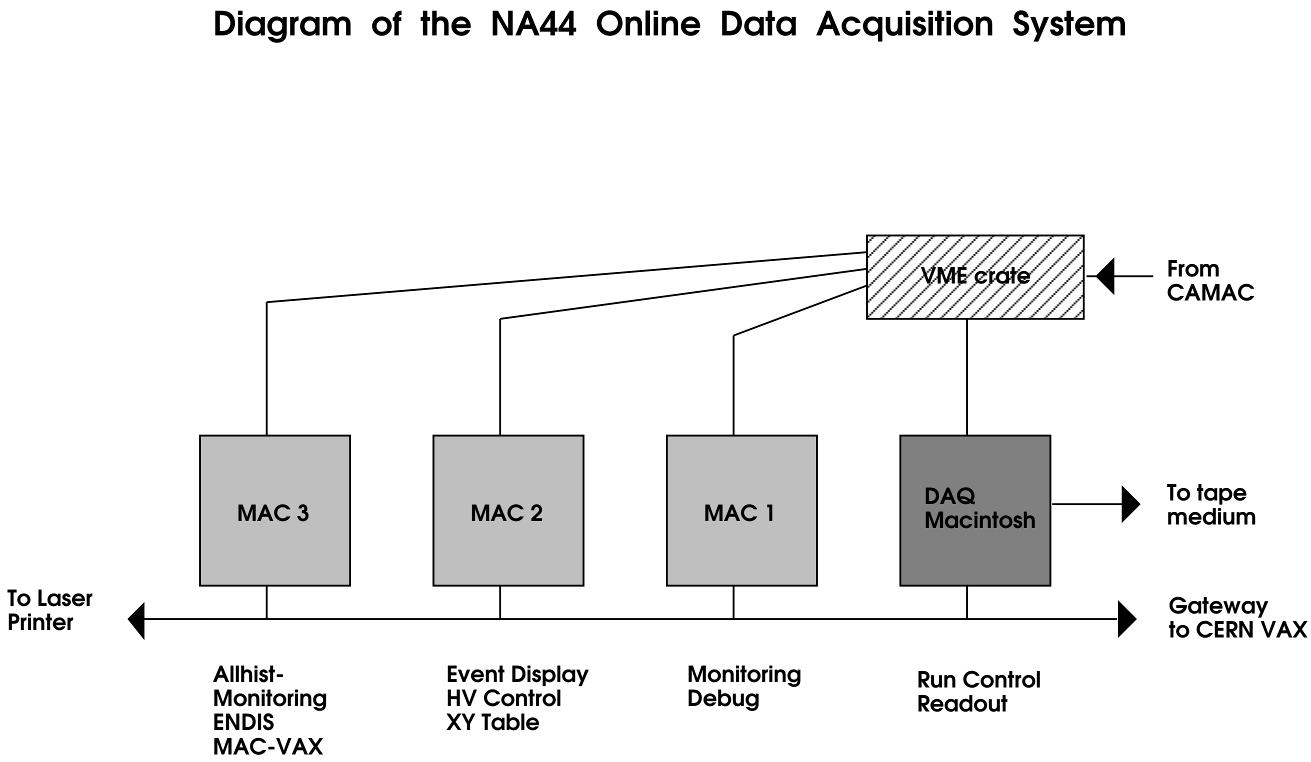

Figure IV-12. The Data Acquisition System.

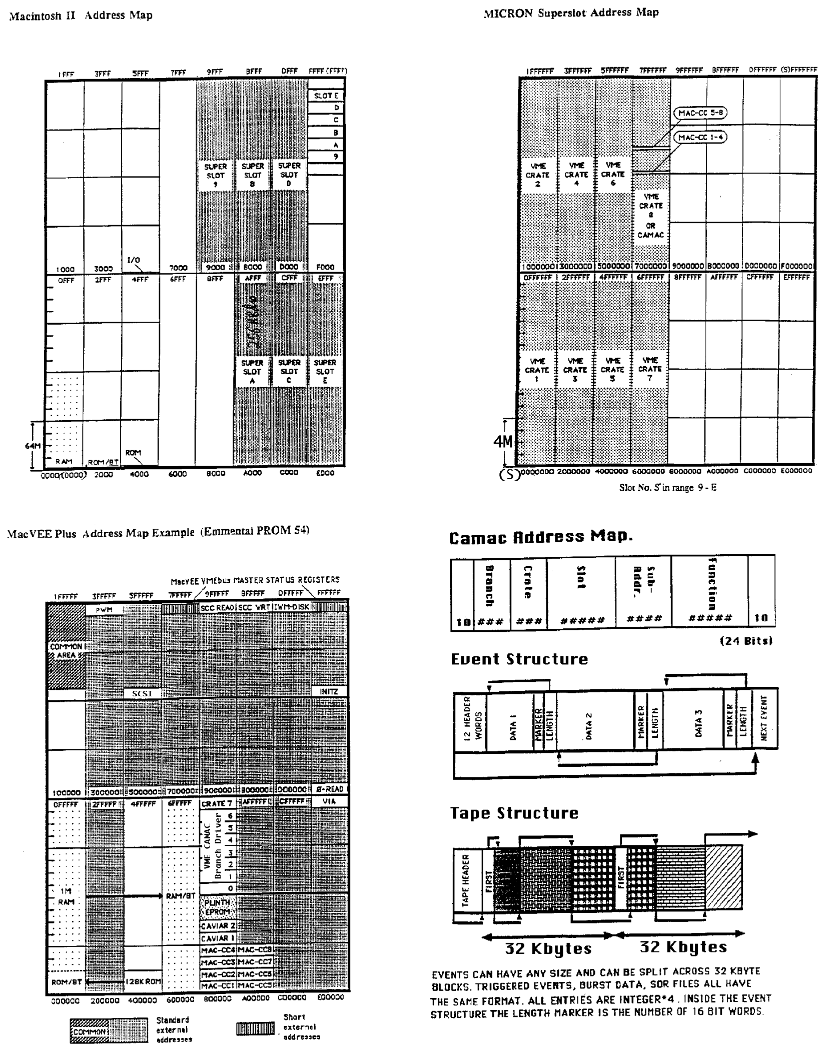

Figure IV-13. Address Maps pertinent to DAQ.

CHAPTER V. Data Reduction and Analysis

The large amount of data that is collected on tape is reduced into momentum vectors after tracking. Most of the analysis , single particle or two-particles, is done with momentum vectors. For single particle inclusive spectra analysis, one is normally interested in the transverse momentum (p_T), while for the pairs analysis the 3-components of the momentum are of interest. The detectors are first calibrated before extracting the hit position information which is used in tracking. The calibrations for the hodoscopes do not depend on any special kind of runs but use the data for the purposes of calibration.

A. Hodoscope Calibrations

The hodoscopes are calibrated either once a day or once every two days or once every running period depending on the constant that one is calibrating. The calibration procedure involves four-passes[Sag92].

In the first pass raw time-of-flight and the pedestals for the ADC are calculated. Raw TOF is calculated as the difference between the average TDC value of each slat of the hodoscope minus the average TDC value of the start-counter. The pedestal is defined as the ADC value that is obtained even in absence of a signal. The pedestal values are subtracted from the measured ADC value slat by slat in order to obtain the true ADC value. Since the pedestals are prone to drifting due to temperature variations these calibrations are performed every two to three days.

Pass 2 and 3 calculate the slewing constants. Since the ADC sets the threshold to the discriminator large ADC pulse heights lead to faster timing and smaller ADC pulse heights lead to slower timings. This effect is corrected for in pass2 and 3. The constants calculated in pass2 and pass3 are dependent on the pass1 constants and

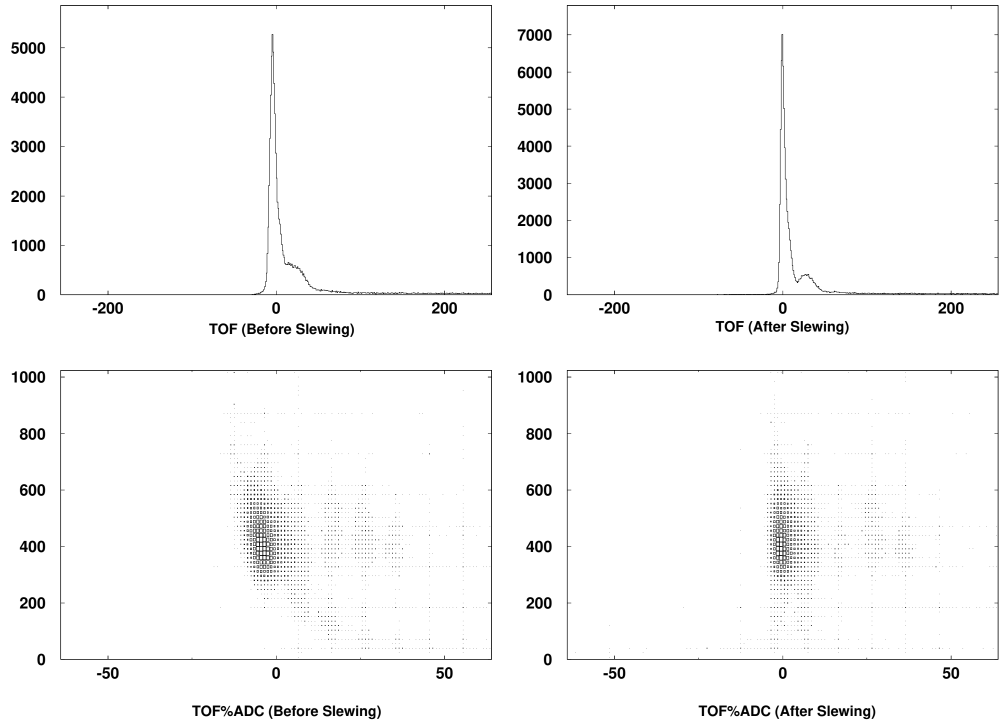

Figure V-1. Time-of-Flight with and without slewing for Hodoscope 2 and 3.

hence their frequency is determined by the pass1 frequency of calibration, which is roughly every two to three days.

$$TOF = 0.5(hTDC_{top} + hTDC_{bot}) - 0.5(TDC_{cx1} - TDC_{cx2}) = A + B/\sqrt{ADC} \quad \text{(V-1)}$$

where A and B are the slewing constants, hTDC refers to hodoscope slat TDC's and TDC_{cx} is the start counter TDC value. The output from pass3 is shown in Figure V-1.

Pass 4 calculates the corrected TOF, ADC gain and the y_{offset}. The corrected TOf is given as

$$TOF_{corr} = TOF + 0.5(\frac{B1}{\sqrt{ADC1}} + \frac{B2}{\sqrt{ADC2}}) + 0.5(\frac{B3}{\sqrt{ADC3}} + \frac{B4}{\sqrt{ADC4}}) \quad \text{(V-2)}$$

where ADC1 and ADC2 are the amount of charge deposited in the top and bottom photomultiplier of the hodoscope slats. ADC3 and ADC4 are the amount of charge deposited on the start counter photomultiplier tubes.

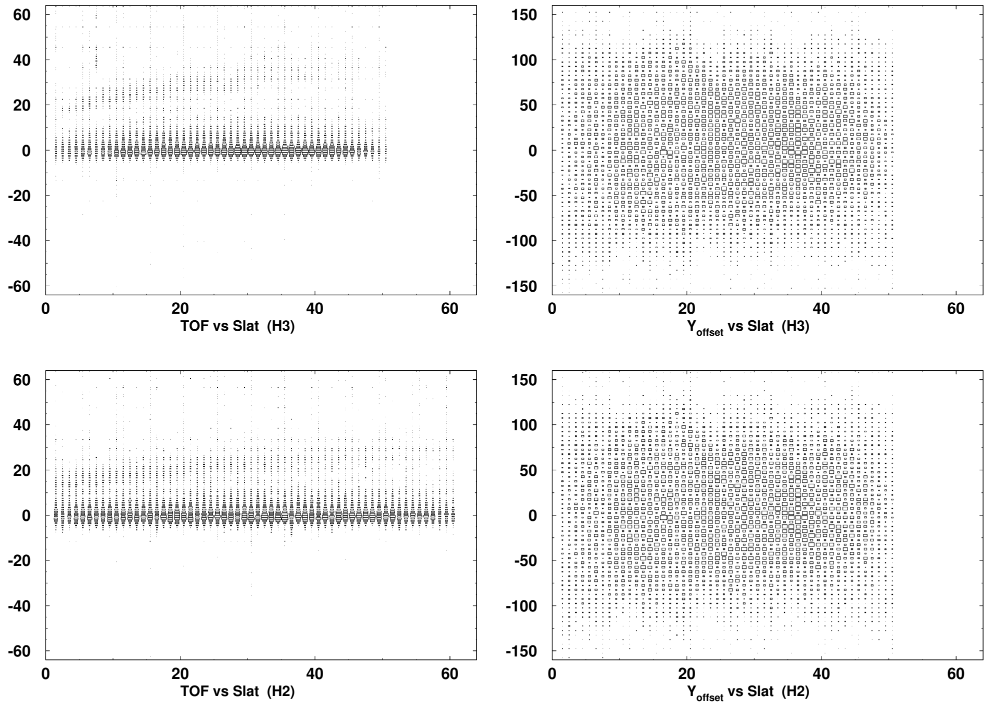

Figure V-2. y_{offset} and T_{offset} for Hodoscope # 2 and #3.

y_{offset} is defined as the crude vertical offset and is given by the equation

$$y = y_{gain} \times (TDC_{bot} - TDC_{top} + y_{offset}) \tag{V-3}$$

where TDC_{bot} and TDC_{top} are the TDC values from the top and bottom photomultiplier of the slat. y_{gain} is calculated using additional information provided by three horizontal scintillators placed behind each of the hodoscopes.

The ADC gain of each photomultiplier is calculated allowing one to renormalize the ADC value of each hit position thus allowing comparisons between the amount of charge deposited in each slat. The time-offset and the y_{offset} from pass4 are shown in Figure V-2.

B. Silicon Pads

The Silicon pad detector sits behind the target and is used as a device to measure the centrality of the collision. For this data set no attempt was made to correct for crosstalk between pads. The minimum ionizing peak is found by fitting the first peak by a Landau distribution. Any pad that has energy greater than this peak is counted as one particle. This crude analysis does permit one to distinguish between central, peripheral and min-bias events.

C. UCAL

The Uranium noise response is calculated by reading the UCAL when there is no beam. This allows one to do gain matching of various subcomponents in the detector. In NA44, only relative calibrations have been performed since the UCAL is used only for the purpose of distinguishing between π,e and μ. The Helios collaboration performed absolute calibrations of this detector [A$^+$87, SG90].

D. Reconstruction

After calibrating the hodoscopes, from the hit positions (x, y, z) on the hodoscopes the tracks are reconstructed and momentum of the track is calculated. The tracks are reconstructed by requiring straight line trajectories tracing back to the exit of the third dipole. The χ^2 is minimized in the x-z and y- z plane. Tracks are never reconstructed when two particles hit the same slat. In case of the first hodoscope if tracks hit adjacent slats then such events are rejected since the geometry of H1 is such that large number of tracks hit adjacent slats. The track reconstruction efficiency is estimated to be $\approx$ 97 %. Further details of the track reconstruction can be found in [Kal93, Pan93, Lee93].

The momentum of the tracks is determined according to the fitted hit positions on the hodoscopes based on a parametrization of known Monte Carlo as discussed in [Lee93].

The propagation of the track through the spectrometer is done by the program called DECAY TURTLE [BI74]. This program allows the simulation of effects like aberrations which exists in beams with small phase-space volume, non-linear effects in magnetic fields and particle decays.

E. Pair files

For the purpose of Bose-Einstein correlations, one requires the four-momentum vectors of the pair of particles. After reconstruction, the ntuple has the momentum information (p_x,p_y,p_z), time of flight information, the Cherenkov ADC value, beam counter ADC and other informations which are useful for cleaning up the data and identify the particle type. From the time-of-flight and momentum of the particle the mass-squared is calculated which enables one to pick the particle species of interest along with the Cherenkov information. Also with the momentum , the slat number on each hodoscope is also written out to the pair data file. This information is important, since if adjacent slats are hit on H1, such events are rejected. In case of BE correlation function if the reals are subjected to a particular analysis cut then backgrounds also need to be subjected to the same events cuts.

F. Correlation Function

The correlation function is defined as

$$C_{raw}(\vec{k_1}, \vec{k_2}) = \frac{A(\vec{k_1}, \vec{k_2})}{B(\vec{k_1}, \vec{k_2})} \tag{V-4}$$

where $\vec{k_i}$ are the particle momenta. The correlation function is constructed in different kinematical variables. In NA44 the variables used are Q_{inv} which is defined as

$$Q_{inv} = \sqrt{Q^2 - Q_0^2} \tag{V-5}$$

this variable assumes a spherical source distribution. One often runs into interpretational problems while using Q_{inv}, details of which will be discussed in chapter V. A second set of variables used in NA44 are $Q_r = \tau$ which is defined as

$$Q_{R=\tau} = \sqrt{Q^2 + Q_0^2} \tag{V-6}$$

This variable assumes a spherically decaying source. One does not however fit to both Q and Q_0 simultaneously, but forces R = τ while performing the fits. This is a useful variable since it allows comparison with other experiments which often perform fits in one-dimension owing to limited statistics. A point to note is that Q_0 is not an independent variable, as shown in appendix B, but is related to $\vec{Q}$

$$Q_0 \approx \frac{\vec{Q} \cdot \vec{K}/2}{\sqrt{(K/2)^2 + m^2}} = \vec{Q} \cdot \vec{V_{K/2}} \tag{V-7}$$

where $\vec{K} = \vec{k_1} + \vec{k_2}$ and $\vec{V}$ is the velocity of the pair in the analysis frame. High statistics allows us to perform three-dimensional fits to our data. The three dimensional correlation function is defined as

$$C(\vec{k_1}, \vec{k_2}) = 1 + e^{-(R_x Q_x)^2 - (R_y Q_y)^2 - (R_z Q_z)^2 - (\tau Q_0)^2} \tag{V-8}$$

Since $q_0 \approx \vec{q} \cdot \vec{V_{K/2}}$ the above equation reduces to

$$C(\vec{k_1}, \vec{k_2}) = 1 + e^{-Q_x^2(R_x^2 + V_x^2 \tau^2 cos^2\theta) - Q_y^2(R_y^2 + V_y^2 \tau^2 cos^2\theta) - Q_z^2(R_z + V_z^2 \tau^2 cos^2\theta)} \tag{V-9}$$

where θ is the angle between $\vec{q}$ and $\vec{K}/2$. The analysis of data in this thesis is done in a frame in which the two particle momentum sum is zero along the beam direction, $K_z = k_{1z} + k_{2z} = 0$ as suggested by Pratt [PCZ90]. This frame is also referred to as the "Longitudinal Center of Mass System" or LCMS. Since one never knows the rest frame of the source, one assumes it to be different from the $K_z = 0$ frame by a Lorentz factor γ in the z direction. The above equation now reduces to

$$C(\vec{k_1}, \vec{k_2}) = 1 + e^{-Q_{t_o}^2 R_{t_o}^2 - Q_{t_s}^2 R_{t_s}^2 - Q_l^2 R_l^2} \tag{V-10}$$

where Q_l is along the beam direction, Q_{t_o} is parallel to the total two particle momentum and Q_{t_s} is perpendicular to both Q_{t_o} and Q_l. Figure V-3 illustrates the kinematic varibles.

The "real distribution", $A(\vec{k_1}, \vec{k_2})$, is the distribution of the relative momentum, and the "Background distribution", $B(\vec{k_1}, \vec{k_2})$, is constructed from mixing events randomly from the real distribution. This distribution should ideally contain all correlations except the Bose-Einstein correlation. The Background distribution is constructed as follows: For each event in $A(\vec{k_1}, \vec{k_2})$, twenty pairs of events from the same run are selected randomly to form the background pairs. In these pairs, one particle in each event is selected randomly to create a new 'event' for the $B(\vec{k_1}, \vec{k_2})$ distribution. Thus statistical uncertainties are dominated by the reals instead of the backgrounds. As in the reals, the background distribution is subjected to the same analysis cuts, ensuring that the reals and the background distributions are from the same class of collisions.

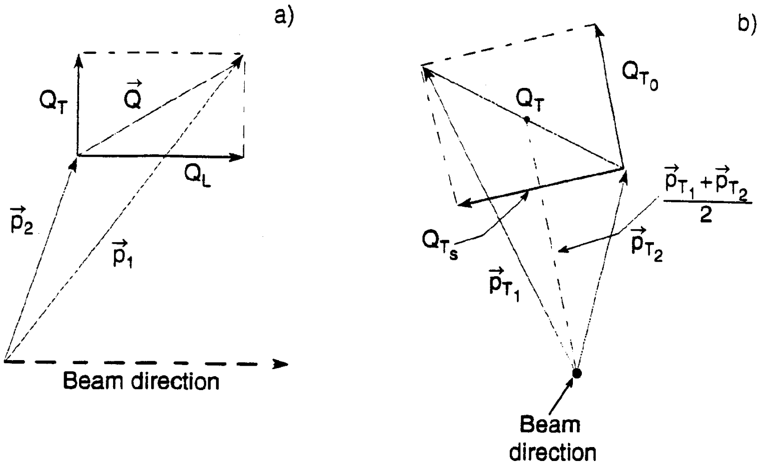

Figure V-3. Kinematic Variables

G. Corrections

The data was corrected for various effects before fitting. The background spectrum is distorted owing to two particle correlations on the single particle spectra. The method of constructing background distribution from real distributions leads to residual correlations in the single particle spectra [B+93a, KS92, Z+82]. This correction is done in an iterative manner and the mathematical details are given in Appendix A. The data was also corrected for momentum smearing and acceptance effects. The following procedure is adopted in this thesis: a list of particles is created from a known event generator [JH87]. The particles are then propagated through the spectrometer by Decay Turtle and the tracks are reconstructed by the Monte Carlo program which simulates the NA44 detectors. Then a list of output particles are created. A correlation function is constructed with the set of input particles and with the set of output particles. The ratio of the two gives the correction factor due to spectrometer inefficiencies and resolution,

$$\frac{C'(Q)}{C(Q)}. \tag{V-11}$$

The above two correction factors depend on the input source radius and hence an iterative procedure is employed. Fit parameters converge in about four to five iterations. The data was further corrected for final state Coulomb interactions, the

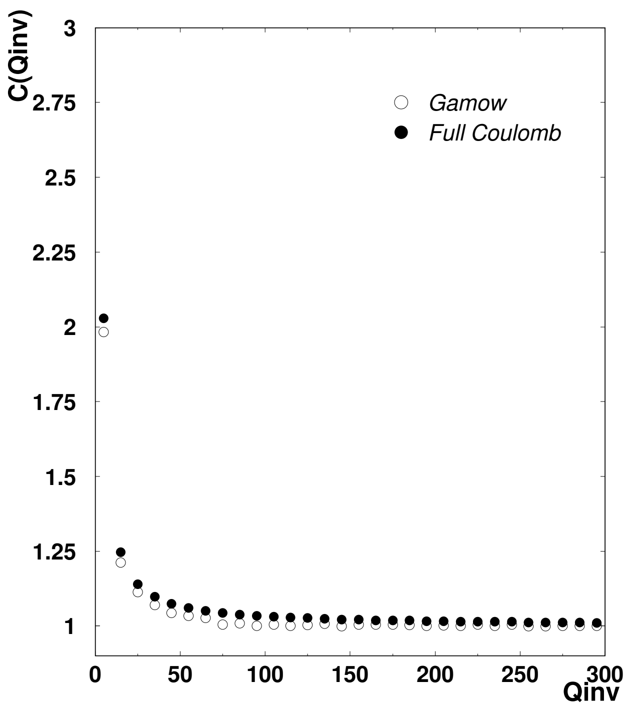

Figure V-4. Simulated Correlation function with Gamow (open circles) and Full Coulomb Corrections (closed circles).

standard Gamow factor is applied at the center of the bin, bin by bin. A more accurate correction factor would result if full Coulomb integrals are evaluated. Applying Coulomb correction instead of Gamow would lead to about a 10% affect on the radius and λ as shown in Figure V-4. Furthermore, applying the correction to mid-bin leads to problems as discussed by [Pan93]. No correction is applied to take in account the Coulomb interactions with rest of the nuclear matter, but these are considered to be less important for particles with identical charge-to-mass ratios which experience similar accelerations in the Coulomb field. No attempt is made to correct for final state strong interactions, but these are important if the emitted particles have different charge-to-mass ratios [BGJ90].

H. Fit functions

The Data was fit using three different Gaussian parametrizations. The fit functions used in this thesis are

$$C(Q_{inv}) = A(1 + \lambda e^{-Q_{inv}^2 R_{inv}^2}) \tag{V-12}$$

$$C(Q_{R=\tau}) = A(1 + \lambda e^{-Q_{R=\tau}^2 R_{R=\tau}^2}) \tag{V-13}$$

and

$$C(Q_{t_o}, Q_{t_s}, Q_l) = A(1 + \lambda e^{-Q_{t_o}^2 R_{t_o}^2 - Q_{t_s}^2 R_{t_s}^2 - Q_l^2 R_l^2}) \tag{V-14}$$

where A is the overall normalization factor and holds no "physical" significance.

One of the methods of fitting is to use least squares method to fit the data. In this method one minimizes the quantity

$$\chi^2 = \sum_i \frac{(C_i - A_i/B_i)^2}{\sigma_{A_i/B_i}^2} \tag{V-15}$$

where the summation is over all the bins. In the limit of low statistics the above method has problems as discussed in detail by [Zaj90]. In the limit of low statistics the ratio of two Poisson distributions is not a Poisson distribution. Hence the error estimate σ_{A_i/B_i} can be a severe underestimate of the actual error [JR80]. Furthermore, χ^2 minimization method assumes a Gaussian distribution of errors which is not valid in the limit of low statistics. One can instead minimize,

$$\chi^2 = \sum_i \frac{(A_i - C_i B_i)}{\sigma_{A_i}^2 + \sigma_{B_i}^2} \tag{V-16}$$

thus avoiding taking ratios of small numbers [Bar89]. However, in the limit of low statistics one still lacks Gaussian distribution of errors. The alternative approach is that of maximum likelihood method, which in the limit of large statistics reduces to χ^2 minimization method. The quantity that is maximized is

$$P(A_i|\overline{A_i} = C_i B_i) = \frac{\overline{A_i}^{A_i}}{A_i!} e^{-\overline{A_i}} \tag{V-17}$$

Hence one no longer takes ratios, but assumes that B_i has negligible errors in comparison with A_i . This assumption is valid since B_i is constructed with 20 times more statistics in comparison with A_i. Hence the quantity maximized is

$$L = \prod_i P(A_i|\overline{A_i}) \tag{V-18}$$

or the quantity minimized is given by

$$-\,ln(L) = \sum_i \overline{A_i} - A_i ln(\overline{A_i}) + ln(A_i!) \tag{V-19}$$

The minimization is done by MINUIT [Jam80]; a package developed at CERN to do fitting and for error estimation on the fitted parameters. For χ^2 method, 1σ errors are calculated by allowing χ^2 to vary by one for a given change in parameters of interest with knowledge of all correlations between the other parameters. For maximum likelihood estimators, the probability that an interval between estimates c_1 and c_2 includes the true value of the parameter is [Mey75]

$$Pr(c_1 \le c \le c_2) = \frac{\int_{c_1}^{c_2} dcL(c)}{\int_{-\infty}^{+\infty} dcL(c)}. \tag{V-20}$$

If $Pr(c_1 \le c \le c_2) = 0.68$, then the limits c_1 and c_2 correspond to one standard deviation.

I. Statistical and Systematic Errors on the Fit Parameters

Statistical errors on the data points are calculated as,

$$\sigma_{C_i} = C_i \sqrt{(\frac{\sigma_{A_i}}{A_i})^2 + (\frac{\sigma_{B_i}}{B_i})^2} \tag{V-21}$$

The errors are assumed to obey Poisson statistics, that is $\sigma_{A_i} = \sqrt{A_i}$. The correlation function is constructed assuming that the correction factors add no additional errors to the statistical fluctuations and is fit with MINUIT, which returns fit parameters with 1σ errors on the fit parameters.

The systematical errors are more difficult to evaluate than the calculation of statistical errors. In this thesis the systematical errors are calculated by varying the analysis procedure and then re-fitting the correlation function to the data. The different analysis cuts employed are (i) Correlation function is constructed by doing a slat cut on just H1, (ii) Correlation function is constructed by doing slat cut on all three hodoscopes, (iii) finally the correlation function is constructed by changing the target thickness to half its value. The error matrix is calculated from

$$V_{if}^{sys} = [\frac{\sum_{k=1}^{N} C_{ik}C_{jk}}{N} - C_i^{mean} C_j^{mean}]\frac{N}{N-1}, \tag{V-22}$$

where N is equal to the number of simulated data sets and

$$V_{ij} = V_{ij}^{sys} + V_{ij}^{stat}, V_{ij}^{stat} = 0; i \neq j \tag{V-23}$$

For out data the correlation coefficient ρ

$$\rho_{ij} = V_{ij}/(V_{ii}V_{jj})^2 \tag{V-24}$$

is less than 0.2 for almost all bins, indicating that the systematic errors have little effect on fits to the data.

J. Presentation of the Data

The presentation of one-dimensional correlation function is rather easy, but problems arise while trying to present the two or three dimensional correlation function. The presentation in this thesis is done [Cha91, Cha90] by averaging over the other two components (for e.g. $Q_{t_s}$and Q_{t_o}), at a given value of Q_o, to display averages of the quantities as a function of Q_o. By using each of the variables in turn, three displays are made showing the data and the fitted correlation function projected onto each of the coordinate axes. Note that these are averages weighted by the spectrometer's acceptance and hence the projection of the data and the fitted function are both distorted by the acceptance. The definition of the data points in the projection (C_k) is given by

$$C_k = \frac{\sum_{ij} R_{ijk}}{D \cdot \sum_{ij} B_{ijk}} \tag{V-25}$$

the uncertainty in the data points is estimated as

$$(\Delta C_k)^2 = C_k^2 \{ \frac{1}{\sum_{ij} R_{ijk}} + \frac{\sum_{ij}(\Delta B_{ijk})^2}{\sum_{ij}(B_{ijk})^2} \}, \tag{V-26}$$

and the fitted curve is given by

$$\langle C_k \rangle = \frac{\sum_{ij} C_{ijk} \cdot B_{ijk}}{\sum_{ij} B_{ijk}} \tag{V-27}$$

where D is the overall normalization constant, R_{ijk} is the real counts per bin, B_{ijk} is the background counts per bin and ΔB_{ijk} is the estimated uncertainty in the background counts per bin. In the above equations the index k is kept, and the first and second indices (i and j) are averaged over. If $R_{ijk} \approx$ D$\cdot C_{ijk} \cdot B_{ijk}$ the curves will be close to the data points.

The other method suggested by Pratt [Pra93] is to increment the bin $k' = \sqrt{i^2 + j^2 + k^2}$ instead of k. In this method one gets the intercept right but distorts the shape of the correlation function.

CHAPTER VI. Results And Discussions

Results of fits in one and three dimensions are presented in this chapter, along with comparisons to model calculations which act as a tool to interpret the extracted parameters.

A. One Dimensional Analysis

Fits in one dimensions use either Q_{inv} or $Q_{R=\tau}$, both the parameterizations assume a spherical source; Q_{inv} assumes a spherical source expanding in time whereas $Q_{R=\tau}$ assume a spherical source decaying in time. The latter being more realistic than the former. Figure VI-1 & VI-2 show the acceptance of the spectrometer for the horizontal and vertical settings. While performing fits in one-dimensions only data from the horizontal setting is taken, since the resolution in the vertical setting is rather poor and the horizontal setting has sufficient acceptance in Q_{inv}. Both Q_{inv} and $Q_{R=\tau}$ have interpretational problems, since they average over all the components of Q, hence the measured R is difficult to interpret. Furthermore $Q^2_{inv} = M^2_{inv}$ - $4m^2$, where m is the mass of the particle. From this equation it is evident that when comparing particles of different masses, it is difficult to interpret the trend seen in R_{inv}.

Fits performed with $Q_{R=\tau}$ are useful in comparing the results at high energies (i.e. CERN energies) with the lower AGS energy experiments, which perform fits in one-dimensions owing to lack of statistics.

Figure VI-3 shows the affect of various corrections on the Correlation function. Even if no corrections are applied the data still shows an enhancement at low Q. The predicted dip at low Q is not seen owing to poor resolution.

Figure VI-4 and VI-5 show the one dimensional Gaussian fits to data. The error bars are small indicating the good quality of the data. From Table 1 and 2 the trend in data is evident. Going from low to high p_T setting the radius parameters

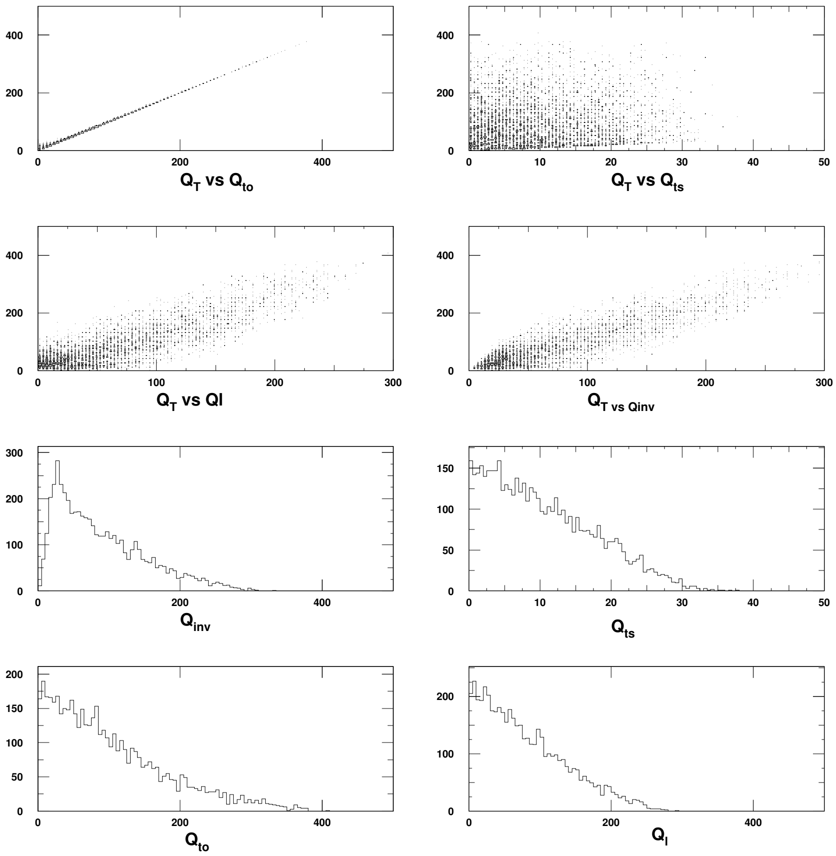

Figure VI-1. Acceptance of the spectrometer in the Horizontal setting.

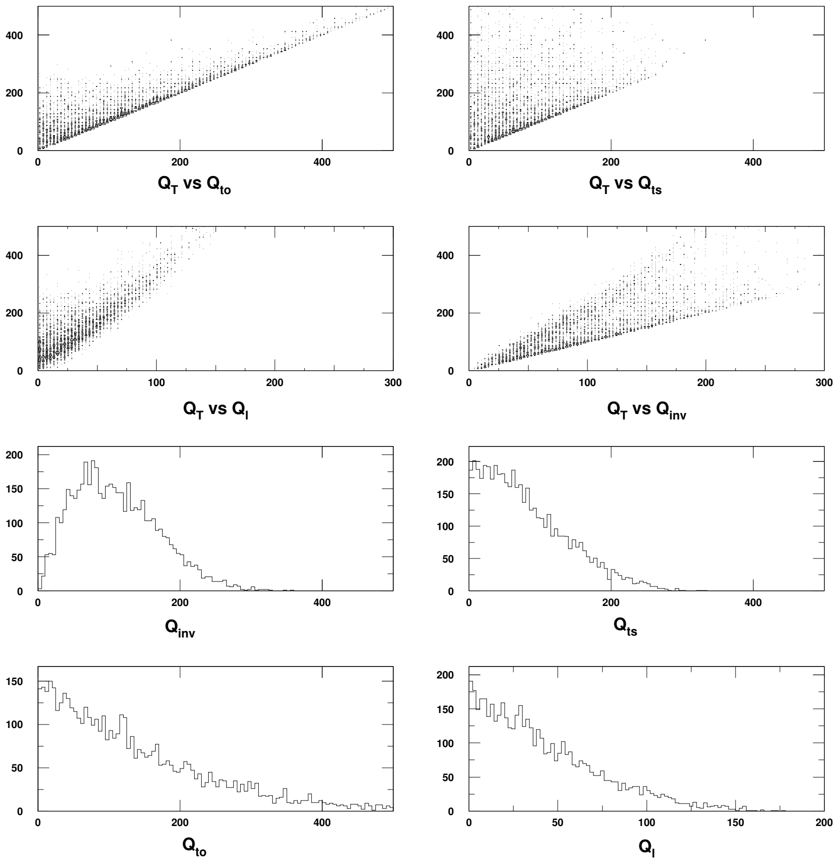

Figure VI-2. Acceptance of the spectrometer in the Vertical setting.

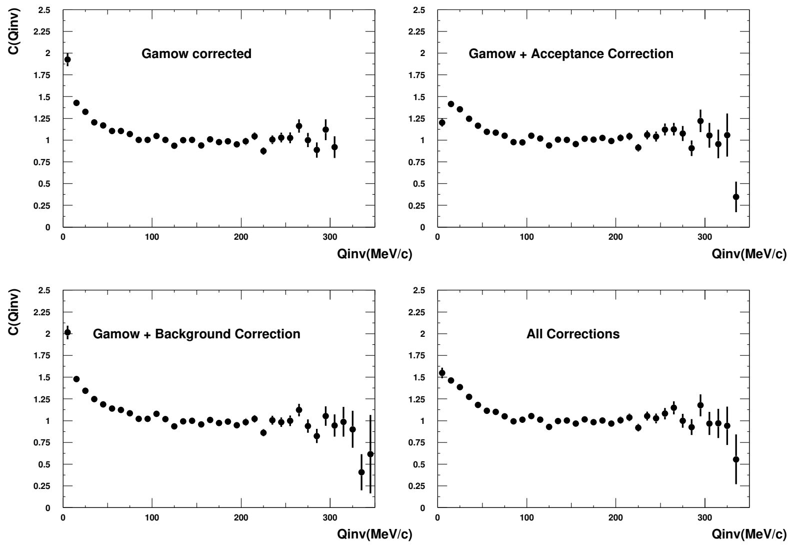

Figure VI-3. Effect of various Corrections on the Correlation Function.

Table VI-1. Results[B+95, B+94a] of Gaussian parameterizations in Q_{inv}. ($< p_T >$ in MeV/c)

System ($< p_T >$)	λ	$R(R = \tau)$ (fm)	χ^2/N_{dof}
$\pi^+\pi^+(\approx 450)$	0.52 ± 0.05	2.36 ± 0.13	42/30
$\pi^+\pi^+(\approx 150)$	0.59 ± 0.03	3.90 ± 0.14	24/25
$K^+K^+(\approx 240)$	0.85 ± 0.06	2.69 ± 0.14	65/36

decrease. The low p_T kaons and the high p_T pions have comparable radii. The lambda parameter however shows no p_T dependence in case of pions.

It is worthwhile mentioning that within 10% errors one cannot distinguish between an exponential radius R and a Gaussian radius $\approx\sqrt{8}$R. It has been pointed out in the earlier surveys that one cannot experimentally distinguish between a uniform spherical distribution and a Gaussian fit, since the correlation curves differ by about 2% for $R_{sphere} = \sqrt{5}R_{gauss}$. Lorstad [Lor89] has shown that the models based on Kopylov and Podgoretski [Kop74] differ from the Gaussian fit by a factor of maybe 2. If the experiment has limited statistics then one cannot distinguish between single and double gaussians.

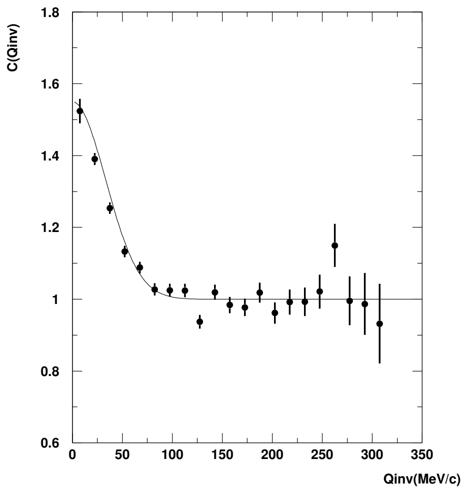

Figure VI-4. Gaussian parametrization in Q_{inv}. The line indicates a Gaussian fit to data points.

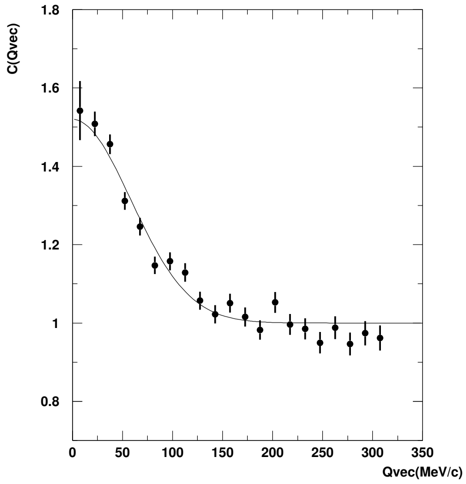

Figure VI-5. Gaussian parametrization in $Q_{r=\tau}$. The line indicates a Gaussian fit to data points.

Table VI-2. Results[B+95, B+94a] of Gaussian parameterizations in $Q_{R=\tau}$. ($< p_T >$ in MeV/c)

System ($< p_T >$)	λ	$R_{R=\tau}$ (fm)	χ^2/N_{dof}
$\pi^+\pi^+(\approx 450)$	0.48 ± 0.02	4.27 ± 0.23	27/20
$\pi^+\pi^+(\approx 150)$	0.56 ± 0.02	5.00 ± 0.22	29/25
$K^+K^+(\approx 240)$	0.92 ± 0.08	3.22 ± 0.20	53/31

B. Three Dimensional Analysis

In order to get a better physical picture of what we measure, one often fit the data with three-dimensional Gaussians. The variables used for the three-dimensional fits are Q_{t_o}, Q_{t_o} and Q_l. Instead of assuming a spherical source distribution, the momentum difference is resolved into components. Since the data is analysed in a frame where the momentum sum along the beam direction is zero, the time component is fully coupled to Q_{t_o} [PCZ90].

Figure VI-1 and VI-2 show the spectrometer acceptance for the horizontal and vertical settings. The acceptance of Q_{t_s} in the horizontal setting is very small hence while fitting in three-dimensions we use data from the horizontal and vertical settings to get the full acceptance for the three components.

Figure VI-6 shows the projection of the three dimensional correlation function. From Table 3, one sees that the trend seen in case of 3-dimensional fits is similar to the trend seen in 1-dimensional fits, namely, the radii decrease going from low p_T to high p_T pions. The kaons and the high p_T pions have similar radii. The lambda parameter shows no p_T dependence for pions. Another interesting thing to note is that $R_{t_o} \approx R_{t_s} \approx R_l$, suggesting a spherical source.

C. Interpretation

How do we interpret the results and trends seen in the data? One way to do this is compare it to model calculations. One such model which simulates heavy-ion collisions is Relativistic Quantum Molecular Dynamics (RQMD) [SSG89]. It is

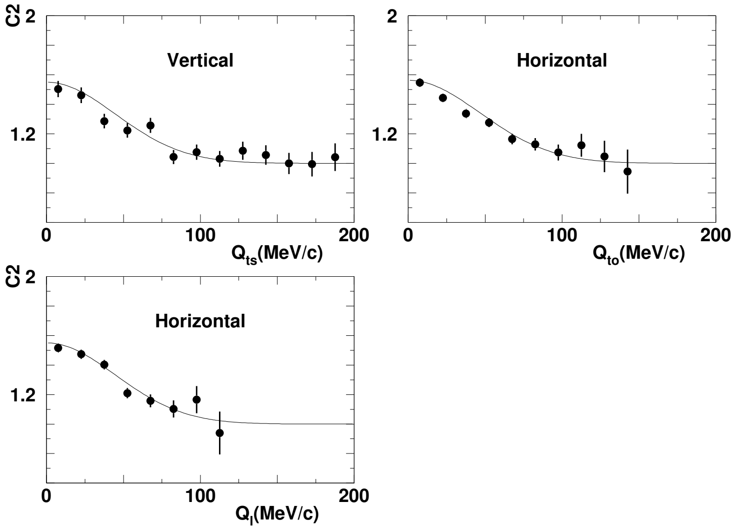

Figure VI-6. Projections of the three dimensional correlation function. The line represents a Gaussian fit to data points.

a model which incorporates rescattering, decays, resonances, string excitation and other effects which are present in a collision.

Given a model which simulates heavy-ion physics, one can create a list of particles at freezeout from this model. The particles are then subject to a given spectrometer acceptance and then a correlation function is calculated with the list of particles which make it through the spectrometer [PCZ90, C$^+$90].

Discussion

Our three dimensional analysis of S+Pb data indicate that within rather small errors

$$R_{t_s} \approx R_{t_o} \approx R_l \tag{VI-1}$$

. These results may be interpreted in the following way:

(i) a first order phase transition, which would lead to R_{t_o} significantly larger than R_{t_s} [BB89, Pra86b], is not borne out in our results.

(ii) the lifetime parameter, τ, which represents the width of freezeout time distribution, is estimated from the static Gaussian model as

$$\tau = \frac{1}{\beta}\sqrt{R_{t_o}^2 - R_{t_s}^2} \tag{VI-2}$$

where β is the average transverse velocity of the particle pair; we find that this time is rather short, i.e. less than a few fermi/c.

It is instructive to compare our measured R_{t_s} parameter to the radius of the projectile nucleus. The equivalent Gaussian radius is given by:

$$R_{gauss} = 1.2A^{1/3}/\sqrt{5}\ \ fm \tag{VI-3}$$

where A is the number of nucleons. The R_{gauss} for sulphur and proton are 1.69 fm and 0.44 fm respectively, both of which are considerably smaller than the measured R_{t_s}. This indicates considerable expansion of the source before freezeout.

A comparison of results from CERN enegeries with those at the AGS energies shows that the R-parameters extracted at the higher energies are larger than those from lower energies. This is indicative of an expanding system which suffers lot of rescattering before freezeout.

We now discuss our observations in the light of two models both of which permit the estimation of geometrical source sizes. Within the framework of the first one, RQMD [SSG89], it is also possible to evaluate the influence of resonances and the experimental acceptance on the R and λ parameters as a function of increasing p_T. This model can also be used for the physical interpretation of the extracted fit parameters which are different from the actual radius and lifetime of the source due to correlations between the particles' momentum and position. These correlations are induced by the expansion of the source driven by particle rescattering [Hum94].

The shape of the $\pi\pi$ correlation is influenced by the $\omega(789)$, its contribution decreasing considerably from low to high p_T [Qua94, B$^+$93b]. The correlation functions predicted by RQMD for our acceptance, however, do not show an appreciable increase in λ, in agreement with the data. In contrast to the low p_T pions, only about 4% of the kaons [S$^+$93b] come from resonances with lifetimes that are long compared to the size of the system. Consequently, the kaon R parameters should be comparable to those of high-p_T pions.

Reasonable agreement of data on high p_T pions with RQMD is shown in Figure VI-7; RQMD and data show similar trends in the R parameters. Because of the correlations between position and momentum, which indicate a collective expansion, the R parameters from the correlation function are in general smaller than the source position distribution. This is true for any experimental acceptance [S$^+$93b]. The

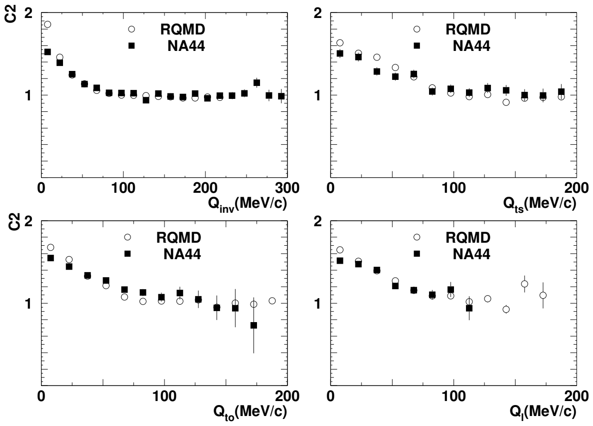

Figure VI-7. Comparison of S + Pb data with RQMD calculations.

agreement with RQMD parameters at large p_T allows us to infer the transverse spatial dimension of the pion source at freezeout. The R_{T_s} parameter calculated from RQMD, which most closely reflects the source transverse size, is 3.25 ± 0.12 fm for high-p_T pions, while the width of a Gaussian fit to the transverse position distribution of high p_T pions at freezeout in the model is 3.5 fm.

Within RQMD, the position distribution of particles at freezeout can be obtained. Figure VI-8 (top plots) shows the position and time distributions at freezeout for pions and kaons. Figure VI-8 (bottom plots) shows the comparison of the correlation function from RQMD to the Fourier transform of the position distributions. One sees a clear disagreement between the Fourier transform and the simulated correlation function. Another point to note is that the position distribution is a non-Gaussian with long tails, indicating that the assumptions that have gone into the construction of a correlation function are incorrect. If momentum and position are correlated, i.e. a particle with a given momentum comes from a given position, then the measured correlation function is not a true Fourier transform of the source distribution function. To elaborate, if one considers a very long source, particles with small momentum difference come from near by in space and hence one is only sensitive to correlations within one unit of rapidity, as a consequence of which the full source is never measured.

We also compare our measurements to a simple hydrodynamical model, which predicts the R parameters to scale as $1/\sqrt{m_T}$ [CL94] for all mesons. The collective

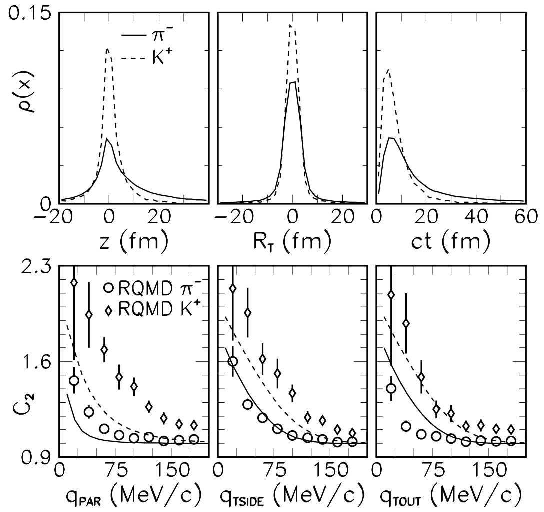

Figure VI-8. Comparison of the RQMD correlation function with source size in the model.

Table VI-3. Results[B+95, B+94a] of Gaussian parameterizations in Q_{t_o}, Q_{t_s} and Q_l. ($< p_T >$ in MeV/c).

System	λ	R_{to} (fm)	R_{ts} (fm)	R_l (fm)	χ^2/N_{dof}
$\pi^+\pi^+(\approx 450)$	0.55 ± 0.02	2.97 ± 0.16	2.95 ± 0.24	3.09 ± 0.19	1500/1095
$\pi^+\pi^+(\approx 150)$	0.56 ± 0.02	4.02 ± 0.14	4.15 ± 0.27	4.73 ± 0.26	1201/1415
$K^+K^+(\approx 240)$	0.82 ± 0.04	2.77 ± 0.12	2.55 ± 0.20	3.02 ± 0.20	925/1011

Table VI-4. Results of the m_T dependence on radius parameter in the LCMS.

System ($< p_T >$)	$\sqrt{m_T}$	$\sqrt{m_T}R_{to}$	$\sqrt{m_T}R_{ts}$	$\sqrt{m_T}R_l$
$\pi^+\pi^+(\approx 450)$	0.68	2.0 ± 0.1	2.0 ± 0.1	2.1 ± 0.1
$\pi^+\pi^+(\approx 150)$	0.47	1.9 ± 0.1	2.0 ± 0.1	2.2 ± 0.1
$K^+K^+(\approx 240)$	0.74	2.1 ± 0.1	1.9 ± 0.20	2.2 ± 0.2

expansion leads to strong momentum-position correlations in both longitudinal and transverse directions [S+92, Qua94]. The velocity gradient together with the freezeout temperature generate a length scale in all three dimensions. If the source length scales are considerably larger than this, for a cylindrically symmetric three-dimensional expansion, the three measured R parameters become equal in the LCMS and show a $1/\sqrt{m_T}$ dependence [CL94]. Our measurements, summarized in Table 3, indicate that, in the LCMS,

$$R_l \approx R_{t_o} \approx R_{t_s} \propto 1/\sqrt{m_T} \qquad \text{(VI-4)}$$

This model implies that the source dimensions are larger than the extracted R parameters from the correlation function.

Both models discussed include a collective expansion, explicitly in the hydrodynamical model, and as a consequence of the rescattering in RQMD. The data indicate the presence of expansion but cannot address the relative validity of the two models.

It should be noted that our result is not a rapidity effect, since the rapidity range for all three data sets in this thesis is between 2.5 - 4.0 and the rapidity density varies only by about 10% [Qua92].

D. Deuterons

Deuterons like pions, kaons and protons can be used to study the source sizes and the collective expansion. The technique to study source sizes using deutrons is different from that used by pions and Kaons.

Deuterons are formed either by direct production or by the coalesence of a proton and a neutron. The threshold for direct production is 15.9 GeV/c hence this is a possible mechanism at both the AGS and CERN energies [A+92]. In the coalesence model, the production of light nuclei follow a power law [C+75]:

$$d/\overline{d}(p^{'}) \approx [p/\overline{p}(p^{'}/2)]^2 \tag{VI-5}$$

where $p^{'}$ is the momentum of the deuteron/antideuteron. The scaling relation ship is given by [Jac85]:

$$E_A d^3\sigma_A/dp_A^3 = B_A[E_P d^3\sigma_P/dp_P^3]^A \tag{VI-6}$$

where A is the fragment mass number, $d^3\sigma_A/dp_A^3$, $d^3\sigma_P/dp_P^3$ are the proton and complex fragment momentum space densities, E_A and E_P are the total energies and B_A is the coalescence scaling factor. According to coalescence, the probability of forming a d in momentum space is proportional to the p density times the probability of a n being located in a small sphere (p_0) around the momentum p [G+76, BP63]. The coalescence radius is expressed as:

$$p_0^3 = (3m\sigma_0/4\pi)B_A[(Z_t+Z_p)/(N_t+N_p)]^N A^2 N!Z!^{1/A-1} \tag{VI-7}$$

where N, N_t, N_p are the fragment, target and projectile neutron numbers; Z, Z_t, Z_p are the fragment, target and projectile proton numbers respectively, m is the nucleon rest mass and σ_0 is the reaction cross-section. The coalesence radius is proportional to the effective source or interaction volume at the time of condensation into clusters. The coalescence radius thus obtained can be compared to the radius obtained from pion HBT. At the Belevac [Jac85] energies it was found that the HBT radius and the coalescence radius are similar.

At the CERN energies, NA44 reports the presence of deuterons and 2 anti-deuteron candidates for the study of source sizes. The single particle m_T or p_T spectra for the deuterons indicates that the slope extracted from the deutrons is

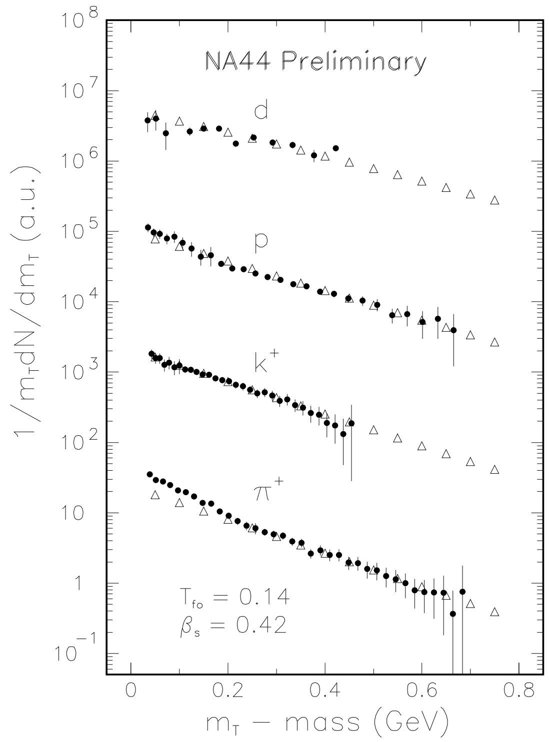

Figure VI-9. Single particle spectra from NA44.

larger than that from protons, implying collective motion. The m_T spectra for various particles is shown in Figure VI-10. The coalesence radius extracted from the SPb collision is 9.9 ± 0.3, which is larger than that measured from HBT. This could arise from various effects such as collective expansion and position-momentum correlations. Coalesence model including position space will lead to a decrease in the measured coalescence radius. The analysis of the pA data shows that the deuteron slopes increase going from pA to AA , and that the coalesence factor increases going from pA to AA. At the Bevalac however it was seen that the coalesence radius was constant with respect to beam energies and projectile types, indicating the breakdown of the simple coalesence model. Coalesence models which take into account the spatial separation between the proton and neutron along with the momentum do tend to reproduce the trend in data.

CHAPTER VII. Conclusions

The Interferometry study of the data from S + Pb Collisions at 200 GeV/n has shown the following trends: *(i)* the extracted radii are larger than the projectile size, *(ii)* the extracted source radii show a p_T or m_T dependence, and *(iii)* the three componenets of the R-parameters are approximately equal to each other within errors, i.e. $R_{t_o} \approx R_{t_s} \approx R_l$. All the above trends seen support the picture of an expanding system which large degree of rescattering of particles before freezeout. The freezeout time extracted from the two transverse R-parameters is rather small indicating either fast decoupling or that the velocity gradient is very steep. However, our interpretation would be greatly modified if there exist momentum-position correlations. A model calculation of the nuclear collision does indicate the presence of strong position-momentum correlations, which arise either from rescattering or from pure kinematics. Thus the data do not however indicate the freezeout time of a QGP since the formation time measured by HBT is of the order of 1 fm/c, which is much shorter than that expected for the QGP.

One expects that the sources measured from Pb + Pb collisions at 160 GeV/c will shed more light on the existing trends. The preliminary Pb data analysed so far does indicate larger pion source sizes but not dramatically larger than expected. However, this data needs a very careful and systematic analysis before drawing strong conclusions. A plot of the preliminary correlation function from Pb + Pb collisions is shown in Figure VII-1.

In short, I have investigated the m_T dependence of boson correlation functions in S+Pb collisions. The R parameters for pions and kaons show a $1/\sqrt{m_T}$ dependence. This dependence can be explained by the presence of strong position-momentum correlations, arising from collective flow. A further investigation of this dependence can be done by careful comparison of hydrodynamical model predictions [S$^+$93a, CL94] to single particle spectra of π, K, p and d, p-p correlations and d/p ratios.

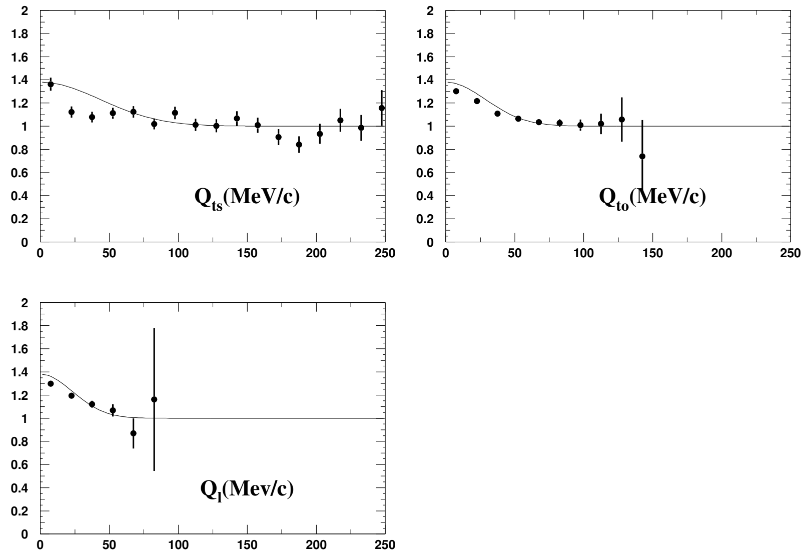

Figure VII-1. Projections of the three dimensional Correlation function for Pb + Pb Collisions at 160 GeV/A (Preliminary).

APPENDIX A. Residual correction to Bose-Einstein Correlation function

As discussed in Chapter 4, the most common presciption used to generate the Background is that of event-mixing [Kop74]. The assumption made in this case is that the background has all correlation except the Bose-Einstein Correlations. But in practice, it is found that event-mixing never fully removes the correlations induced by Bose statistics. Failure to remove these effects can lead to spurious conclusions concering the degree of pion source, coherence etc. The technique used in this thesis is as follows:

As discussed earlier the correlation function is constructed by

$$C_{(2)}(k_1, k_2) \equiv \frac{\langle P(k_1, k_2)\rangle}{\langle P(k_1)\rangle\langle P(k_2)\rangle}. \tag{A-1}$$

However, we construct our background distribution from the real distribution, hence

$$Background = \langle P(k_1)_n\rangle\langle P(k_2)_n\rangle \tag{A-2}$$

where

$$\begin{aligned}
\langle P(k_1)_n\rangle &= \int dk_2\, \langle P(k_1, k_2)\rangle && \text{(A-3)}\\
&= \langle P(k_1)\rangle \int dk_2\, \langle C(k_1, k_2)\rangle\langle P(k_2)\rangle && \text{(A-4)}\\
&= \langle P(k_1)\rangle \int dk_2\, (1 + \Lambda(k_1, k_2)\langle P(k_2)\rangle && \text{(A-5)}\\
&= (1 + \epsilon(k_1)\langle P(k_1)\rangle && \text{(A-6)}
\end{aligned}$$

Thus

$$C_{(2)}(k_1, k_2)^n = \frac{C_{(2)}(k_1, k_2)}{(1 + \epsilon(k_1))(1 + \epsilon(k_2))}. \tag{A-7}$$

However, since we do not know $C_{(2)}(k_1, k_2)$ or $\langle P(k_1)\rangle$ we use an iterative process to calculate these constants namely

$$\langle P(k_1)_n\rangle = \langle P(k_1)_0\rangle \int dk_2\, \langle C(k_1, k_2)_{n-1}\rangle\langle P(k_2)_{n-1}\rangle \tag{A-8}$$

and

$$C_{(2)}(k_1, k_2) \equiv \frac{\langle P(k_1, k_2)\rangle}{\langle P(k_1)_{n-1}\rangle\langle P(k_2)_{n-1}\rangle}. \tag{A-9}$$

This iterative process converges to stable values for the extracted source parameters within two to four iterations.

One sees that the above corrections are really independent of the origin of two particle correlations. Rather, they derive from the assumed form of the correlation function in Equation A-5. Further, even in the limit of a 4π detector these correction terms exist. One can also see from Equation A-5 that if the acceptance of ones spectrometer populates the region primarily where the correlation function is most pronounced the correction factors will be larger. Hence small acceptance spectrometer experiments are particularly susceptible to these corrections.

APPENDIX B. Q_0 is an dependent variable.

Allowing the following definitions:

$$\vec{P} = \frac{\vec{P}_1 + \vec{P}_2}{2} = \frac{\vec{K}}{2} \tag{B-1}$$

$$\Delta\vec{P} = \frac{\vec{P}_1 - \vec{P}_2}{2} = \frac{\vec{Q}}{2} \tag{B-2}$$

one can calculate the energies of both particles using the definitions

$$W = \frac{2\vec{P}\cdot\Delta\vec{P} + (\Delta\vec{P})^2}{\vec{P}^2 + m^2} \tag{B-3}$$

$$V = \sqrt{P^2 + m^2} \tag{B-4}$$

$$E_1 = \sqrt{(\vec{P} + \Delta\vec{P})^2 + m^2} = V\sqrt{1 + \frac{1}{2}W} \tag{B-5}$$

$$E_2 = \sqrt{(\vec{P} - \Delta\vec{P})^2 + m^2} = V\sqrt{1 - \frac{1}{2}W} \tag{B-6}$$

One can Taylor expand these terms

$$E_1 = V\Big(1 + \frac{1}{2}W - \frac{1}{8}W^2 + \cdots\Big) \tag{B-7}$$

$$E_2 = V\Big(1 - \frac{1}{2}W + \frac{1}{8}W^2 + \cdots\Big) \tag{B-8}$$

and since $Q_o = E_1 - E_2$

$$Q_o = V\Big(2\vec{P}\cdot\Delta\vec{P}/V^2 + \frac{1}{8V^4}[-4(\vec{P}\cdot\Delta\vec{P}) - 4(\vec{P}\cdot\Delta\vec{P})] + \cdots\Big) \tag{B-9}$$

$$Q_o = 2\vec{P}\cdot\Delta\vec{P}/V - (\vec{P}\cdot\Delta\vec{P})\Delta\vec{P}^2/2V^3 + \mathcal{O}(\Delta\vec{P}^6/V^5) \tag{B-10}$$

$$Q_o = \vec{Q}\cdot\vec{v}_{\vec{K}/2}(1 - \vec{Q}^2/16V + \mathcal{O}(\vec{Q}^4/128V^3) + \cdots) \tag{B-11}$$

Hence one sees that $Q_o \approx \vec{Q}\cdot\vec{v}_{\vec{K}/2}$.

APPENDIX C. Kinematical Variables.

The mathematical definitions of various kinematical variables frequently used in the heavy ion physics community are presented in this Appendix.

Transverse momentum is considered to be directly created by the collision and is defined as

$$p_T = psin(\theta) \tag{C-1}$$

where p is the momentum of the particle and θ is the angle the particle makes with the beam axis. Similarly transverse energy is defined as

$$E_T = Esin(\theta). \tag{C-2}$$

These variables are relativistically invariant to boosts along the beam axis. The longitudinal momentum p_L, however, is not relativistically invariant to boosts along the beam axis hence the rapidity y, defined as

$$y = \frac{1}{2} ln \frac{E + p_L}{E - p_L} = arctan(v_L/c) \tag{C-3}$$

is often used, as a Lorentz boost along the beam axis corresponds to a constant shift in rapidity. Note that in the center of mass frame $p_L = 0$ corresponds to $y = 0$ (central rapidity). This variable is used to characterize what part of collision one is looking at, as shown in Figure C-1.

The central rapidity of two colliding objects of different mass is defined as the frame in which the net longitudinal momentum is zero. At the CERN SPS for equal mass target and projectile, the central rapidity in the laboratory frame is $y = 3$.

For massless particles or for $E >> m$ one can replace p_L by $Ecos(\theta)$ giving

$$y' = \frac{1}{2} ln \frac{1 + cos(\theta)}{1 - cos(\theta)} = ln(cot(\theta/2)) = \eta \tag{C-4}$$

Note that this is a function only of the scattering angle θ in the laboratory.

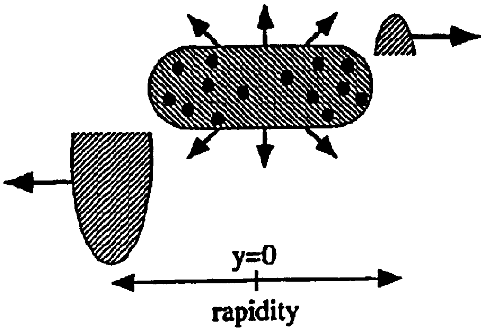

Figure C-1. Rapidity.

BIBLIOGRAPHY

[A+87] T. Akesson et al. Performance of the Uranium/plastic scintillator calorimeter for the Helios experiment at CERN. *CERN-PPE/87-111*, 1, 1987.

[A+90] T. Abbott et al. Kaon and pion production in central Si+Au collisions at 14.6 A Gev/c. *Z. Phys. Rev. Lett.*, 64, 1990.

[A+91a] S. Abatzis et al. λ and $\bar{\Lambda}$ production in sulphur-tungsten interactions at 200 GeV/c per nucleon. *Phys. Lett.*, B244:130, 1991.

[A+91b] T. Abbott et al. Comparison of p+A and Si+Au collisions at 14.6 A GeV/c. *PHys. Rev. Lett.*, 66, 1991.

[A+92] M. Akoi et al. Measurement at 0 of negatively charged particles and antinuclei produced in collisions of 14.6gev/c si on al, cu and au targets. *Phys. Rev. Lett.*, 69, 1992.

[B+90] A. Bamberger et al. Neutral Strange particle production in Sulphur-Sulphur and proton-Sulphur collisions at 200 GeV/nucleon. *Z. Phys.*, C48, 1990.

[B+93a] H. Beker et al. *Phys. Lett. B*, 302, 1993.

[B+93b] J. Bolz et al. . *Phys. Rev.*, D47, 1993.

[B+94a] H. Beker et al. Kaon interferometry in heavy-ion collisions at the cern sps. *Z. Phys.*, C64, 1994.

[B+94b] H. Beker et al. m_T dependence of bosom interferometry in heavy ion collisions at the cern sps. *Phys. Rev. Lett.*, 1994.

[B+95] H. Beker et al. Directional Dependence of Identified pion interferometry at the CERN SPS. *Phys. Lett. B*, 1995.

[Bar89] R. Barlow. Fitting the ratios of two distributions. *CERN/EP 89-40*, 1, 1989.

[BB89] G. Bertsch and G. E. Brown. Temporal development of the plasma phase transition. *Phys. Rev.*, C40, 1989.

[Bek90] H. Beker. A Small Physics Acquisition and Analysis Workstation. *CERN-PPE*, 1990.

[BGJ90] H. Boal, C. Gelbke, and B. Jennings. Intensity interferometry in subatomic Physics. *Rev. Mod. Phys.*, 62, 1990.

[BGT88] G.F. Bertsch, M. Gong, and M. Tohyama. Pion interferometry in ultra-relativistic heavy-ion collisions. *Phys. Rev.*, C37, 1988.

[BI74] K.L. Brown and Ch. Iselin. Decay turtle. February 1974. CERN 74-2.

[Bow85] M. G. Bowler. Bose-Einstein symmetrization, coherence and chaos; with particular application to e^+e^- annihilation. *Z. Phys.*, C29, 1985.

[Bow87] M. G. Bowler. On surprises from Bose-Einstein correlations. *Oxford Preprint OUNP 65/87 (1987)*, 1, 1987.

[Bow90] M. G. Bowler. Extended sources, final state interactions and Bose-Einstein Correlation. *Z. Phys.*, C39, 1990.

[BP63] S. T. Butler and C. A. Pearson. Deutrons from high-energy proton bombardment of matter. *Phys. Rev. Lett.*, 129, 1963.

[C+75] J. W. Cronin et al. Production of hadrons at larger transverse momentum at 200, 300 and 400 gev. *Phys. Rev. D*, 11, 1975.

[C+90] T. Csörgő et al. *Phys. Lett.*, B241, 1990.

[Cha90] A. D. Chacon. *Investigation of the Space-Time Evolution of the Interaction Region in Heavy Ion Collision using Bose-Einstein Interferometry Techniques.* Ph.D. Thesis, University of California, August 1990.

[Cha91] A. D. Chacon. *Phys. Rev. C*, 43, 1991.

[CL94] T. Csörgő and B. Lörstad. Bose Einstien Correlations for Three Dimensionally Expanding Cylindrically Symmetric Finite Systems. *LUNFD6/(NFFL-7082)*, 1, 1994.

[ER91] K. Eggers and J. Rafelski. Strangeness and quark gluon plasma: Aspects of theory and experiment. *preprint AZPH-TH/90-28*, page 1, 1991.

[Flü74] S. Flügge. *Practical Quantum Mechanics*. Springer-Verlag, Berlin, 1974.

[G+76] H. Gutbord et al. Final state-interactions in the production of hydrogen and helium isotopes by relativistic heavy ion on uranium. *Phys. Rev. Lett.*, 37, 1976.

[GK81] M. Gyulassy and S. K. Kauffmann. Dynamic verses symmetrization in hadron interfeometry. *Phys. Rev. Lett.*, 48, 1981.

[GKW79] M. Gyulassy, S. K. Kauffmann, and Lance W. Wilson. Pion interferometry of nuclear collisions. *Phys. Rev.*, C20, 1979.

[GP90] M. Gyulassy and M. Pluemer. Jet quenching in dense matter. *Phys. Lett.*, B243, 1990.

[H+91] H. Van Hecke et al. Measurement of kaons in the Helios experiment. *Nucl. Phys.*, A525:227c, 1991.

[HB+52] R. Hanbury-Brown et al. Apparent angular sizes of discrete radio sources. *Nature*, 170, 1952.

[HBT56] R. Hanbury-Brown and R. Q. Twiss. A test of a new type of stellar interferometer on Sirius. *Nature*, 178, 1956.

[Hof87] W. Hofmann. *LBL-23108*, 1, April 1987.

[Hum94] T J Humanic. Multiple scattering effects on boson interferometry in high energy heavy-ion collisions. *Phys. Rev. C*, 50, 1994.

[J+93] R. Jayanti et al. A documentation on the na44 on-line monitoring system. *NA44 documentation*, 1, 1993.

[Jac85] B. V. Jacak. Coalescence of complex fragments. *Phys. Rev. C*, 31, 1985.

[Jam80] F. James. *Comp. Phys. Comm*, 20, 1980.

[JH87] A. D. Jackson and H.Boggild. A model of transverse energy production in high energy nucleus- nucleus collisions. *Nucl. Phys.*, A470, 1987.

[JR80] F. James and M. Roos. *Nucl. Phys.*, B172, 1980.

[Kal93] H. Kalechofsky. *Identified Single Charged Particle Production in Relativistic Heavy Ion Collisions at the CERN Super Proton.* Ph.D. Thesis, University of Pittsburgh, July 1993.

[Kop74] G. I. Kopylov. Like particle correlations as a tool to study the multiple production mechanism. *Phys. Lett. B*, 50, 1974.

[KS90] T. Kobayashi and T. Sugitate. Test of prototypes of a highly-segmented TOF hodoscope. *Nucl. Instr. and Meth.*, A287, 1990.

[KS92] K. Kadija and P. Seyboth. The nonstatistical fluctations and low P_T phenomena caused by Bose-Einstein correlations. *Phys. Lett. B*, 287, 1992.

[Lee93] Y. Y. Leey. *Bose-Einstein Correlation of High Energy Heavy Ion Collisions at CERN SPS.* Ph.D. Thesis, University of Pittsburgh, September 1993.

[Lor89] B. Lorstad. Boson Interferometry – a review of high energy data and its interpretation. *Mod. Phys.*, A4, 1989.

[LP83] M. Lev and B. Petersson. *Z. Phys.*, C21:Nuclear Effects at Large Transverse Momentum in a QCD Parton Model, 1983.

[M+94] N. Maeda et al. Cherenkov beam counter for ultra-relativistic heavy-ion experiments. *Nucl. Instr. and Meth.*, A346, 1994.

[Mey75] S. Meyer. *Data Analysis for Scientist and Engineers*, 20, 1975.

[Nis94] S. Nishimura. *Investigation of the Space-Time Evolution of the Interaction Region in Heavy Ion Collision using Bose-Einstein Interferometry Techniques.* Ph.D. Thesis, Hiroshima University, August 1994.

[Pan93] S.U. Pandey. *Investigation of the Space-Time Evolution of the Interaction Region in Heavy Ion Collision using Bose-Einstein Interferometry Techniques*. Ph.D. Thesis, University of Pittsburgh, August 1993.

[PCZ90] S. Pratt, T. Csörgő, and J. Zimányi. Detailed predictions for two-pion correlations in ultrarelativistic heavy-ion collisions. *Phys. Rev.*, C42, 1990.

[Pra86a] S. Pratt. Coherence and Coulomb effects on pion interferometry. *Phys. Rev.*, D33, 1986.

[Pra86b] S. Pratt. Pion interferometry of quark-gluon plasma. *Phys. Rev.*, D33, 1986.

[Pra93] S. Pratt. *NA44 Note - 126*, 1, 1993.

[Qua92] *Proceedings of the Eighth International Conference on Ultrarelativistic Nucleus-Nucleus Collisions-Quark Matter 1991*, 1992.

[Qua94] *Proceedings of the Eighth International Conference on Ultrarelativistic Nucleus-Nucleus Collisions-Quark Matter 1991*, volume A566, 1994.

[S$^+$92] B. R. Schlei et al. *Phys. Rev.*, B293, 1992.

[S$^+$93a] E. Schnedermann et al. Thermal phenomenology of hadrons from 200 A Gev S + S collisions. *Phys. Rev.*, C48, 1993.

[S$^+$93b] J.P. Sullivan et al. Bose-Einstein Correlations of Pion Pairs and Kaon Pairs from Relativistic Quantum Molecular Dynamics. *Phys. Rev. Lett.*, 70, May 1993.

[Sag92] A. Sagaguchi. *NA44 Note - 95*, 1, 1992.

[Sch92] J. Schukraft. Ultra-relativitic heavy-ion collisions: Searching for the quark-gluon plasma. *CERN-PPE/92-92*, 1, 1992.

[SG90] J Simon-Gillo. The setup and calibration of the na44 uranium calorimeter, NA44 note111. 1, 1990.

[Shu73] E. V. Shuryak. The Correlations of Identical Pions in Multibody Production. *Phys. Lett.*, 44B, 1973.

[SSG89] H. Sorge, H. Stöcker, and W. Greiner. Relativistic Quantum molecular Dynamics Approach to Nuclear Collisions at Ultrarelativistic Energies. *Nucl. Phys.*, A498, 1989.

[Suz87] M. Suzuki. *Phys. Rev. D*, 35, April 1987.

[Z+82] W. A. Zajc et al. Two-pion correlations in heavy ion collisions. *Phys. Rev.*, C29, June 1982.

[Zaj82] W.A. Zajc. *Two-pion correlations in heavy ion collisions*. Ph.D. Thesis, University of California, Berkeley, Nuclear Science Division, Lawrence Berkeley Laboratory, August 1982.

[Zaj90] W. A. Zajc. *Workshop on Correlations and Multi-Particle Production (CAMP)*, 1, 1990.